Long-term and long-distance deformation in submarine volcanoclastic sediments: Coupling of hydrogeology and debris avalanche emplacement off W Martinique Island

Jaume Llopart, Sara Lafuerza, Anne Le Friant, Roger Urgeles, Louise Watremez

Received: 20 January 2021 | Accepted: 25 January 2021

DOI: 10.1111/bre.12553

RESEARCH ARTICLE

Basin Research | IAS EAGE | WILEY

Long-term and long-distance deformation in submarine volcanoclastic sediments: Coupling of hydrogeology and debris avalanche emplacement off W Martinique Island

Jaume Llopart[1,2] | Sara Lafuerza[2] | Anne Le Friant[1] | Roger Urgeles[3] | Louise Watremez[4]

[1]Equipe des Systèmes Volcaniques, Institute de Physique du Globe de Paris, Paris, France

[2]Institut des Sciences de la Terre de Paris, Sorbonne Univertisté, Paris, France

[3]Institut de Ciències del Mar, CSIC, Barcelona, Spain

[4]UMR 8187, LOG, Laboratoire d'Océanologie et de Géosciences, Univ. Lille, CNRS, Univ. Littoral Côte d'Opale, Lille, France

Correspondence
Jaume Llopart, Institut de Ciències del Mar, CSIC, Barcelona, Spain.
Email: jaume.llopart@gmail.com

Funding information
Labex UnivEarthS; PREST project co-funded by INTERREG Caraïbes for the European Regional Development Fund

Abstract

West off Martinique (Lesser Antilles), the Grenada Basin submarine sediments were affected by the emplacement of Debris Avalanche Deposits (DAD). Montagne Pelée Volcano has experienced three major flank collapses during the last ca. 127 kyrs, resulting in a cumulated volume of up to 300 km^3 offshore. Using a combination of geophysical and geotechnical data, we investigate the effect of these debris avalanches emplacements on the basin hydrogeology and their relationship with the observed sediment deformation in the seismic and coring data. The geotechnical test carried on IODP-340 cores samples reveal four sediment types within the basin with distinctive mechanical and hydraulic properties: proximal volcanoclastics, distal volcanoclastics, hemipelagic and ash-rich sediments. These results, together with margin stratigraphic models obtained from seismic reflection data, were used as inputs for the numerical finite-element model. This model shows that the coupling of the sediment properties with the mid- to low-sedimentation rates results in the development of low overpressures prior to the first flank collapse at 127 ka. However, the emplacement of the first two DADs, between 127 and 36 ka, developed high overpressures ratios ($\lambda^* > 0.9$) in the easternmost part of the Grenada Basin. According to the model, the sudden compaction of the pre-existing sediments due to the DADs load created fluid flow velocities up to 7 times higher than the hydraulic conductivities, which would have thus reduced the sediment bearing capacities and shear strength, favouring their mobilization and deformation. From 127 to 36 ka, the sea-floor sediments suffered a long-term deformation driven by the combination of the weight of the emplaced material and the persistence of high overpressure ratios through time. This deformation propagated tens of kilometres away from the DAD's emplacement and it is possible that still continues today due to the persistence of low overpressure ratios. This long-term and long-distance deformation and persisted overpressures are a key factor to take into account in the framework of a geohazards evaluation in areas recurrently affected by earthquakes and volcanic flank collapses.

Journal Name BRE | Manuscript No. 12553 | WILEY | No. of pages: 23 | Dispatch: 11-2-2021 | PE: Maheswari S. | CE: Hari Hara Sudan K

1 | INTRODUCTION

Volcanic islands have an intrinsic potential for high-energy landslide generation due to their high relief and steep slopes. Volcano flank collapses are among the largest onshore to offshore landslide events on our planet (Masson et al., 2006). The most voluminous events have occurred in the past on volcanic islands such as Hawaii, La Reunion, Montserrat or the Canary Archipelago, with landslide deposits ranging from hundreds to thousands of cubic kilometres. (Krastel et al., 2001; Le Friant et al., 2011; Lebas et al., 2011; Moore et al., 1994; Oehler et al., 2008; Urgeles et al., 1999). Nevertheless, even small flank collapse like the most recent Anak Krakatau collapse can cause devastating consequences (Williams et al., 2019). The material of these volcano flank collapses have often partly or almost entirely entered the sea as debris avalanches with volumes exceeding 5,000 km^3 as in Hawaii (Moore et al., 1994). Nonetheless, these onshore to offshore debris avalanches in steeped slopes are not only restricted to volcanic islands, but also in fjords and lakes (Moernaut & De Batist, 2011; Van Daele et al., 2013; Watson et al., 2017). The sudden entrance of such slides into seas, lakes or fjords results in complex subaquous mass movements. The Grenada basin, west off Martinique island, suffered the occurrence of three debris avalanches emplacement during the last 127 kyrs resulting in a submarine landslide deposit with an estimated total volume of ca. 300 km^3 (Brunet et al., 2016). However, the dynamic of the running debris avalanches and the downslope propagation of subaquous sediments deformation are still under debate (e.g. Watt, Talling, Vardy, Masson, et al., 2012). So, conceptual models have been proposed to explain the downslope propagation such as: (a) erosion and loading of seafloor sediment by volcanic debris avalanche, (b) self-loading by down-slope propagating seafloor-sediment failures or c) long-distance decollement propagation from the debris avalanche loading area (e.g. Bull et al., 2009; Watt, Talling, Vardy, Heller, et al., 2012). In turn, the resulting geometry of the deposits can be defined as frontally confined or frontally emergent (Frey-Martínez et al., 2006) with a lobate to circular sea-floor expression depending on the dynamics of the debris avalanche. As a result, thrusted and folded structures can be identified in the sediments affected by this debris avalanches deposition (Watt, Talling, Vardy, Masson, et al., 2012).

The overloading due to these landslides deposition may disrupt the stress and fluid flow fields in the submarine sediments of adjacent basins. Migration of interstitial fluids is mainly controlled by sediment load and hydraulic properties of the different materials. The rapid changes in the distribution of such load, e.g. debris avalanches, can result in the development of excess pore pressures or overpressures and, in turn, result in sediment instability (Dimakis et al., 2000; Micallef et al., 2009; Urlaub et al., 2013). In addition,

Highlights

- Contrasting physical properties between volcanoclastics, hemipelagics and ash-rich sediments.
- Low overpressures developed on submarine sediments before the first volcano flank collapse.
- The Montagne Pelée volcano flank collapses had a major impact on the overpressure generation.
- The observed deformation coincides with high overpressures development that persisted through time.
- The developed high fluid flow velocities decrease the shear strength favouring sediment deformation.

Hornbach et al. (2015) postulated that pore pressures could rise at the toe of these debris avalanche deposits through regional strain and grain reorganization resulting from shear due to earthquake-induced shaking. Hence, favouring the idea that these thrusted and folded structures were induced by long-term deformation of the sediments. However, it is still unclear if such deformation occurred over a long period such as of a few hundreds to thousands years, or if it was rather instantaneous and induced by an almost undrained deposition of the debris avalanches on top of the previous sediments. Although previous works demonstrated an increase in sediments instability with an overpressure build up, some remaining questions need to be addressed: (a) how big and fast has to be the loading by the debris avalanches on the pre-existing sediments in order to cause the observed deformation?; (b) is it necessary to account for a low-to-mid overpressures before the debris avalanches emplacement to trigger such deformation and which is the role of the overpressure build up? and (c) can the load by the debris avalanches on the pre-existing sediments cause a long-range deformation?

The aims of this study are therefore: (a) to characterize the physical and mechanical properties of the Grenada Basin sediments west off Martinique, (b) to model the pore pressure evolution of the sea-floor sediments prior to the flank collapses and (c) to investigate the effect of debris avalanches emplacement on the basin hydrogeology along with the influence of the long-term overpressure persistence and the basin sediments deformation.

2 | GEOLOGICAL SETTING

The Lesser Antilles island arc results from the westward subduction of the Atlantic oceanic crust beneath the Caribbean

plate (Westercamp et al., 1972). North of Dominica, the arc is divided into two chains. To the south, these two chains are superimposed forming a single chain of islands bordered to the west by the 2,900-m-deep back-arc Grenada Basin. This basin has been a major depocenter for volcanic, turbiditic, hemipelagic and large mass-wasting deposits (Boudon et al., 2007; Deplus et al., 2001). Arc volcanism has been active since 40 Ma (Bouysse et al., 1985), but it was not until the Oligocene (24.8–20.8 Ma) that the volcanic activity started in the easternmost part of Martinique Island (Germa et al., 2011; Westercamp et al., 1990). A shift in of volcanic activity towards the north of the island occurred around ca. 5.2 Ma when the region changed from a submarine to subaerial volcanic setting (Germa et al., 2010). During the last 5 Myrs, the volcanism in the northern part of the island has been periodically active, and in particular in the northernmost part from 550 ka to Present (Germa et al., 2010, 2011; Vincent et al., 1989).

The Montagne Pelée volcano in Martinique experienced three major flank collapse events during the last ca. 127 kyrs, which created horseshoe-shaped scars and removed up to tens of cubic kilometres of the western subaerial flank of the volcano (Figure 1 and Figure S1). Le Friant et al. (2003) estimated that the volumes of missing material associated with these flank collapses were about 25 km^3, 13 km^3 and 1.8 km^3 respectively. However, more recent estimations (Poulain et al., 2020) suggest smallest volumes for the two oldest flank collapses (17 km^3 and 9 km^3). It is worth pointing out the difficult to estimate these volumes due to erosion processes and filling of the horseshoe-shaped collapse scars by more recent products. Each flank collapse generated a debris avalanche that deposited on the Grenada Basin. Debris Avalanche Deposits (DAD) are expressed in the bathymetric data as distinct lobes: a) the first two events (DAD1 and DAD2) form a single lobe; and b) a unique lobate deposit occurs for the last one (DAD3) (Figure 1b). The ages of the three flank-collapses have been estimated at 127, 127–45 and 45–30 ka respectively (Brunet et al., 2016; Germa et al., 2011; Le Friant et al., 2015). Recent data from IODP cores (Solaro et al., 2020) suggest that the last flank collapse occurred at 36 ka.

Further to the debris avalanche deposits, a Submarine Landslide Deposit (SLD) has been identified offshore Martinique (Brunet et al., 2016) (Figure 1a). The SLD extends ca. 40 km beyond the debris avalanche deposits (Figure 1) and includes the previous described D1 and D2 deposits by Le Friant et al. (2003). The SLD has been interpreted to result from sea-floor sediment failures and propagation of the deformation induced by the submarine emplacement of the debris avalanches related (Brunet et al., 2016). The SLD body, with an estimated volume of ca. 300 km^3, shows thrust-and-fold structures in places, whereas in other areas it displays highly deformed and reworked sediments (see figure 10 in Brunet et al., 2016). Hornbach et al. (2015) postulated that pore pressures could rise at the toe of the SLD through regional strain and grain reorganization resulting from shear due to earthquake-induced shaking. Hence, favouring the idea that these thrusted and folded structures were induced by

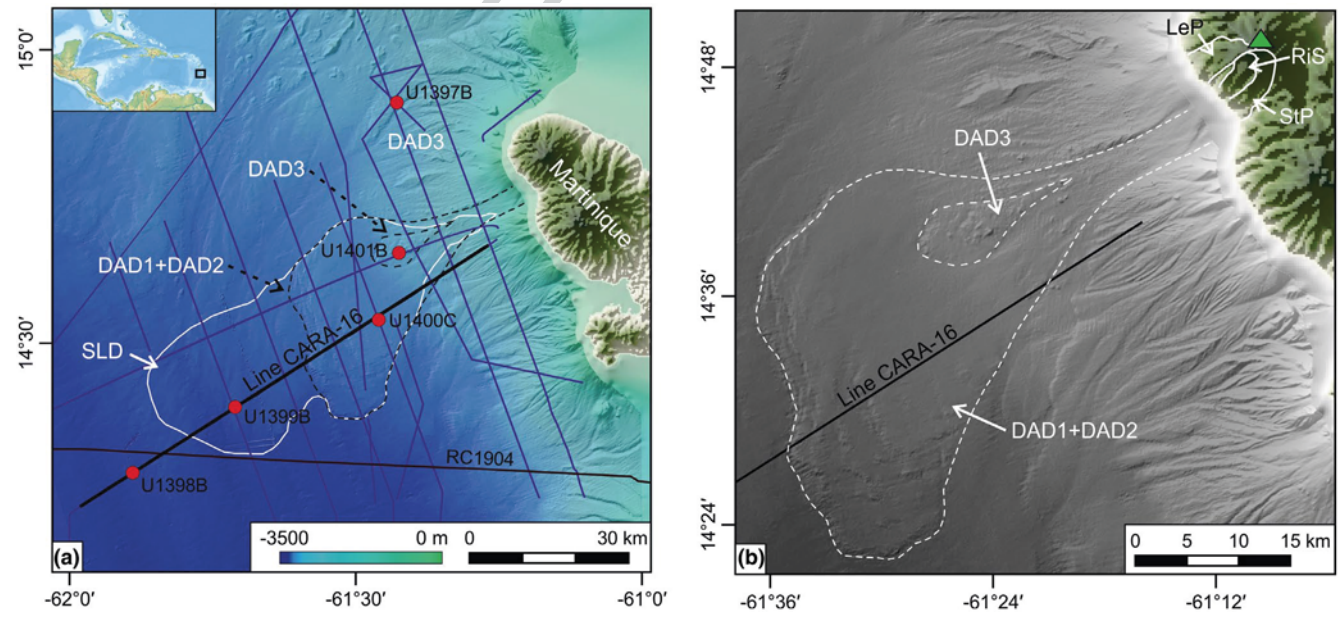

FIGURE 1 (a) Shaded relief showing the seismic profiles from AGUADOMAR, CARAVAL and GWADASEIS cruises (purple lines); sites from IODP Leg 340 (red dots); seismic profile RC-1904 (grey line) and Submarine Landslide Deposit (SLD) from Brunet et al. (2016) (white line). (b) Shaded relief bathymetry and topography showing the morphological expression of the Debris Avalanche Deposits (DAD) from Le Friant et al. (2015) (dashed white lines); the Montagne Pelée flank collapses (white lines): Le Prêcheur (LeP: 127 ka), St. Pierre (StP: 127–45 ka) and Rivière Sèche (RiS: 36 ka); and Montagne Pelée (green triangle)

COLOUR online, B&W in print

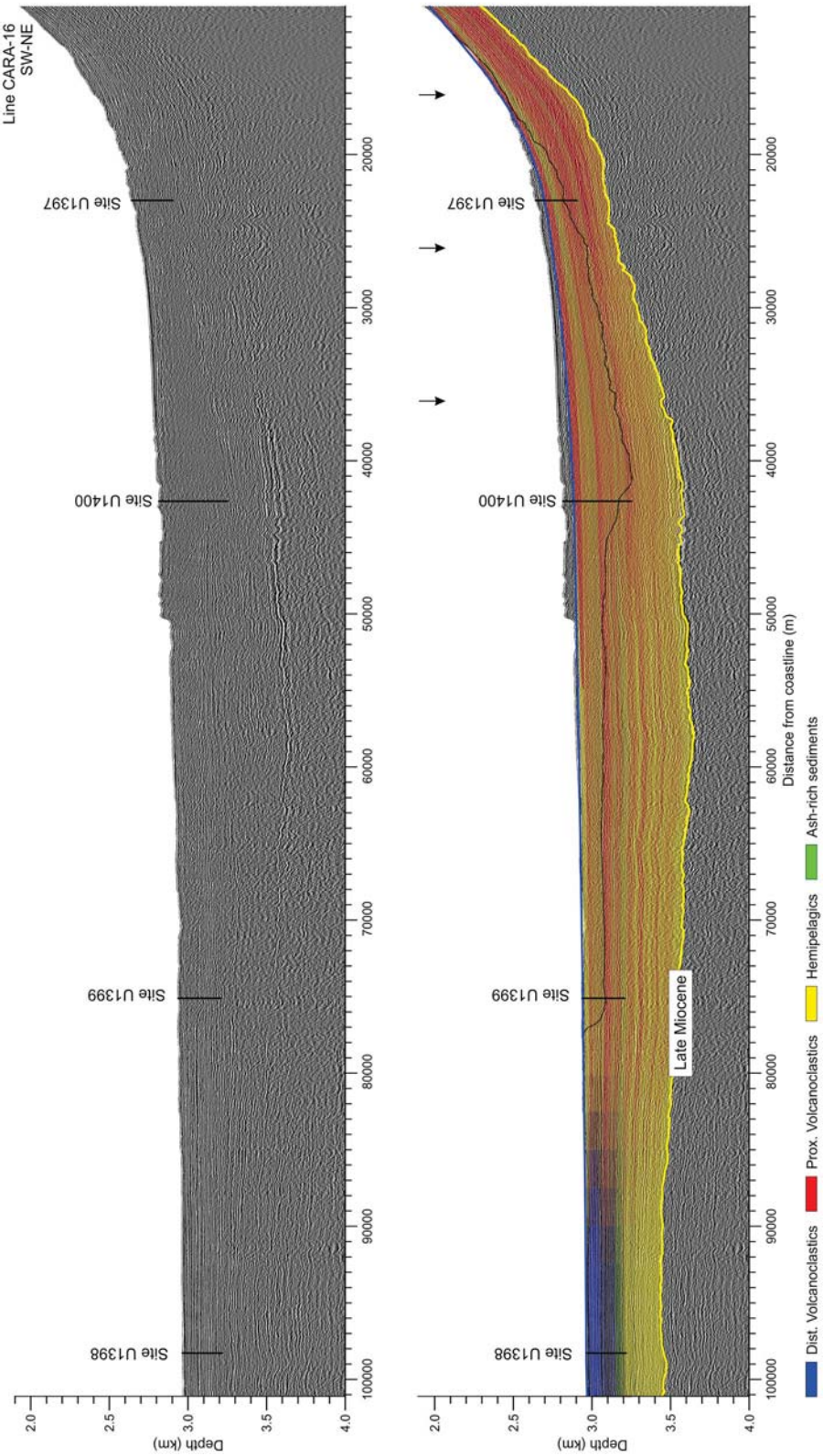

FIGURE 2 Top: Seismic profile CARA-16. Bottom: sediment facies averaged every 13-25m. Colour grading indicates mixing of the original sedimentary facies based on their relative abundance within the layer. Late Miocene (11.2 Ma) reflector (yellow), the reconstructed sea floor (blue) and the base of the deformed sediments (black). Locations of sites from IODP Leg 340 are shown. The IODP U1397 is projected on the profile from its current location (see Figure 1). Black arrows show the location of the synthetic wells at 16, 26 and 36 km distance along the model. VE 10:1

long-term deformation of the sediments. However, it is still unclear if such deformation occurred over a long period such as of a few hundreds to thousands years, or if it was rather instantaneous and induced by an almost undrained deposition of the debris avalanches on top of the previous sediments. Furthermore, the pore pressure state of the pre-existing sea-floor sediments prior to emplacement of the DADs is still unknown and it is crucial to constrain while assessing geo-hazards offshore Martinique Island.

3 | DATA AND METHODS

3.1 | Geophysical and geological data set

The data sets used in this study were collected during four coordinated cruises: AGUADOMAR (R/V L'Atalante, December 1998 to January 1999), CARAVAL (R/V L'Atalante, 2002), GWADASEIS (R/V Le Suroît, 2009) and IODP-340 Expedition (Figure 1). The multi-channel seismic reflection profiles acquired in the study area were gathered using a 6-, 24- and 72-channel streamer (see, e.g. Brunet et al., 2016; Lebas et al., 2011). Each seismic data set was filtered, stacked and migrated at sea water velocity (1,500 m/s) after NMO correction, using the Seismic Unix software (Cohen & Stockwell, 1996). Interpretation of the seismic reflection data was performed using the IHS Kingdom Suite© software. Our study focuses on seismic profile CARA-16 (Figure 1) and uses as a base the interpretation shown in previous works (e.g. Brunet et al., 2016; Deplus et al., 2001; Le Friant et al., 2003). The base of the studied sedimentary sequence is the reflector corresponding to the base of the Late Miocene (Aitken et al., 2011). To constrain the geometry of the base of the Late Miocene reflector in areas of poor imaging along profile CARA-16, the legacy RC-1904 survey acquired in 1975 has been used (Talwani et al., 1977). The processing of this line was limited to NMO and stacking. The time-to-depth conversion has been performed using P-wave velocity logs from the IODP-340 Exp. boreholes (Friant et al., 2013a, 2015). To reconstruct the sea-floor morphology prior to the first avalanche, the entire seismic and bathymetric data available have been used to remove the bathymetric effect of the DADs.

3.2 | Sedimentary and geotechnical data

Sedimentological and geotechnical information used in this study is derived from sites U1397, U1398, U1399 and U1400 drilled during IODP-340 Expedition (R/V Joides Resolution, March–April 2012) offshore Montserrat and Martinique islands (Friant et al., 2013a, 2015). The lithological interpretations (Figure S2) together with logging data (Gamma Ray, P-wave velocity and Magnetic Susceptibility) have been used to assign sedimentary facies along the profile CARA-16 (Figure 1), which together with seismic reflector configuration characterize margin architecture (Figure 2). Data from sites U1397, U1398, U1399 and U1400 have been correlated between cores along the entire profile. The data from site U1397 have been projected to line CARA-16. At site U1400, only the shallower 30 m have been used for the sedimentary architecture reconstruction due to severe deformation and remobilization below these 30 m (e.g. Brunet et al., 2016). From the base of the cores to the base of the model (Late Miocene reflector), sedimentary facies have been tentatively assigned accounting for the transition from a nonvolcanic to a volcanic-influenced setting (Aitken et al., 2011; Germa et al., 2010, 2011).

Consolidation and permeability tests were performed on 19 whole-round samples obtained at depths ranging between 4 and 176 mbsf from holes 1397B, 1398B, 1399B and 1400C; samples are named as the hole-core section (e.g. 1397B-3H2) (see Table 1, Figure 1 and Figure S1). Consolidation tests were carried out in two laboratories: Fugro (France) and the Institut de Ciencies del Mar (CSIC, Spain). At Fugro stepped loading tests were performed using a manually loaded oedometer, whereas at CSIC stepped loading consolidation tests were carried out using a GDS Rowe & Barden-type consolidation

TABLE 1 Geotechnical tests performed on whole-round samples

Hole	Core	Depth (m)	Geotech Lab	Test type
1397B	3H2	18.63	ICM	R&B + K
1397B	3H2	18.66	ICM	CRS
1398B	7H1	42.7	ICM	CRS
1398B	9H4	62.7	ICM	R&B + K
1398B	9H4	63.3	ICM	CRS
1399B	1H3	4.02	ICM	R&B + K
1399B	1H3	4.21	ICM	CRS
1399B	4H4	3,055	ICM	R&B + K
1399B	6H3	46.54	Fugro	SL + K
1399B	13H1	102.7	Fugro	SL + K
1399B	19H3	138.9	Fugro	SL + K
1399B	24H2	162.2	Fugro	SL
1399B	27H2	176.1	Fugro	SL
1400C	3H4	27.21	ICM	CRS
1400C	5H6	47	Fugro	SL
1400C	7H2	61	Fugro	SL
1400C	10H4	84	Fugro	SL + K
1400C	13H4	109	Fugro	SL + K
1400C	19H4	159	Fugro	SL

Abbreviations: CRS, Constant Rate of Strain; K, Permeability test; R&B, Stepped loading Rowe & Barden-type; SL, Stepped loading test.

cell equipped with three 3 MPa pressure/volume controllers. In this oedometer type, a permeability measurement was carried out after each consolidation step inducing a pressure gradient between both sides of the specimen allowing for the determination of permeability using Darcy's law. Further to these tests, Constant Rate of Strain consolidation tests (CRS) were performed at CSIC using a GDS CRS cell within a 50 kN load frame equipped with two 2 MPa pressure/volume controllers and a 25 kN submersible load cell. The strain rate in the CRS tests was set to prevent excess pore pressures higher than 15% of the applied load. These tests have been performed according to the British Standard Methods for soil testing (British Standards Institution, 1990).

3.3 | Finite-element software BASIN

The Finite Element Software BASIN (Bitzer, 1996, 1999) has been used to carry out long-term hydrogeological modelling of the volcanic-influenced continental margin west off Martinique Island and to simulate fluid migration and pore pressure development. The BASIN software is based on a forward modelling approach; for a given set of initial and boundary geological conditions, the evolution of the sedimentary basin is calculated. Compaction and fluid flow are coupled through the consolidation equation and the nonlinear form of the equation of state for porosity, allowing non-equilibrium compaction and overpressure to be calculated (Bitzer, 1999). Instead of empirical porosity-effective stress equations, a physically consistent consolidation model is applied which incorporates a porosity-dependent sediment compressibility. The consolidation equation incorporating porosity-dependent sediment compressibility and hydraulic conductivity is solved using Equation (1):

$$(\partial/\partial x)\left(k_{x(\varnothing)}\partial p/\partial x\right)+(\partial/\partial x)\left(k_{z(\varnothing)}\partial p/\partial z\right)=(1-\varnothing)\,\rho g\alpha_{(\varnothing)}\partial p/\partial t \quad (1)$$

where $k_{x(\phi)}$ is the porosity-dependent hydraulic conductivity in the x-direction, $\alpha_{(\phi)}$ is the porosity dependent sediment compressibility, p is the fluid pressure and ϕ is the porosity.

Sediment compressibility in BASIN is calculated from the specific storage (S_s) using Equation (2):

$$S_s=\rho_s g a \quad (2)$$

Where ρ_s is the sediment density, g is the gravity constant and α is the sediment compressibility.

In this study, pore pressure is described in terms of overpressure ratio (λ^*), defined according to Flemings et al. (2008) as:

$$\lambda^*=\left(p-P_h\right)/\left(\sigma_v-P_h\right) \quad (3)$$

where p is the pore pressure, P_h is the hydrostatic pressure and σ_v is the lithostatic or total stress.

Thus, the rate of overpressure generation depends on the stratigraphic architecture, sedimentation rate, sediment compressibility and permeability. The initial thickness (H_i) of the different strata used as input for the model was calculated using van Hinte's decompaction equation (Van Hinte, 1978):

$$H_i=H_f[\,(1-\phi_f)/(1-\phi_0)\,] \quad (4)$$

where ϕ_0 is the initial porosity at deposition, ϕ_f is the Present-day porosity and H_f is the Present-day sediment thickness.

3.3.1 | BASIN model set up

The total length of the modelled transect along seismic profile CARA-16 is 91.2 km (Figure 1), which is simulated using a mesh that is 40 cells in the x-direction. The stratigraphic model includes 38 layers with an initial thickness ranging between 13 and 25 m. Thus, the horizontal resolution of the model is ca. 2.3 km and the vertical resolution depends on the thickness of individual layers. BASIN allows for a maximum of four sediment types, which have been selected according to the sediment interpretation from previous authors (Brunet et al., 2016; Lafuerza et al., 2014) and physical properties obtained in this study. However, sedimentary facies can be represented by a mixture of the four sediment types, whose composition varies according to their relative abundance for a given area and stratigraphic unit. Physical properties are then averaged at each mesh cell according to the relative abundance of the sedimentary facies in the sediment mixture. The left and right model boundaries are constraint so that only vertical displacements are allowed (neither horizontal nor fluid flow). The bottom boundary of the model is vertically and horizontally fixed and is considered impervious. Only vertical deformation is allowed within BASIN.

To better understand and constrain the role of debris avalanche deposits emplacement in pore pressure build-up, two models have been set: (a) the Grenada Basin evolution from the Late Miocene to Present day without accounting for any avalanche occurrence, and (b) the evolution of the same basin accounting for the loading induced by the submarine debris avalanches resulting from the three volcano flank collapses. The second scenario has been set up with concurrent emplacement of DAD1 + DAD2 at 127 ka and DAD3 at 36 ka. Due to a lack of consensus on the timing of occurrence of the DAD1 and DAD2, the effects of their emplacement on previous sediments will be investigated as part of the uncertainty analysis in section 5.3. Previous authors have found that the volume of collapsed material estimated from the most recent flank collapse (36 ka) from on land observations and the deposit DAD3 were similar, ca. 1.8 km^3 (Brunet et al., ,2016,

2017; Le Friant et al., 2003). Thus, it is expected that the volume of material deposited offshore associated with the first two flank-collapses sensu stricto (DAD1 + DAD2) may, most likely, be similar to the volume of missing material estimated on land. As the joint volume of DAD1 + DAD2 cannot be deduced from seismic data alone (Figure 1), we use the difference between Present-day sea floor and that of an interpolated sea floor within the lobe from the surrounding area not affected by the debris avalanches emplacements. The volume of the DAD1 + DAD2 estimated using this approach is ca. 23.5 km^3, which is smaller than the volumes of the on-land volcano flank collapses (38 km^3, Le Friant et al., 2003). Taking into account the uncertainties arising from subsequent erosion and filling of the structures, 23.5 km^3 can be used as a minimum estimate for the total DAD1 + DAD2 volume. The run-out of the submarine debris avalanches is constrained by the run-out/volume relationship from Brunet et al. (2017) numerical simulations indicating that the emplacement of DAD1 + DAD2 reach ca. 42 km from the coast, and DAD3 ca. 30 km (35 and 23 km in line CARA-16, see Figures 1 and 2). DAD3 has been used to calibrate the amount of decompaction of the material involved in the debris avalanche necessary to produce the Present-day compacted deposit. Finally, the shapes of the older deposits (DAD1 and DAD2) have been inferred from DAD3.

4 | RESULTS

4.1 | Seismic facies and sediment distribution

According to Brunet et al. (2016), seismic line CARA-16 (Figure 2) shows three differentiated facies: well-bedded, disrupted and chaotic. The well-bedded facies correspond to high-amplitude, continuous and subparallel reflectors. The disturbed facies show subparallel to contorted discontinuous reflectors with mid to high amplitude. The chaotic facies are characterized by highly disrupted and with a very low amplitude to acoustically transparent. The well-bedded facies correspond to undisturbed marine sediments, also including the undisturbed drape on top of the sedimentary column (Figure 2 and Figure S2). The proximal and central part of the profile show a body mainly characterized by chaotic facies extending up to ca. 47 km from the coastline and with a maximum thickness of ca. 300 m. This body corresponds to the central part of the SLD and to DAD1 + DAD2 identified by previous authors (e.g. Brunet et al., 2016). The base of the SLD corresponds to a high-amplitude reflector that separates chaotic and well-bedded facies below (Figure 2). This reflector ramps up 150–200 mbsf around 40 km from the coast line and continue subparallel to the sea floor for ca. 30 km where abruptly climbs. At the same time, the facies of the previously described SLD change from chaotic in the central part to disrupted westwards. The deeper most high-amplitude reflector has been identified as the base of the Late Miocene (Figure 2).

Here, we define the sedimentary architecture along profile CARA-16 based on the IODP well data together with the seismic facies interpretation. According to the IODP cores descriptions, the sediments present in the study area consist in very fine-to-coarse volcanoclastic sands, ash, hemipelagics, calcareous ooze and mudstone (Brunet et al., 2016; Figures 9, 10 and 11; Le Friant et al., ,2013b, 2015) (Figure S2). The two more proximal sites U1397 and U1400 are characterized by an upper part (ca. 100 m) mainly composed by volcanoclastic sediments including fine-to-coarse grained turbidites with variable silt and clay content, interbedded with hemipelagics and ash layers (Brunet et al., 2016 Figure 11) (Figure S2). From 100 to ca. 150 m, hemipelagic sediments are the prevailing sediment type with some ash and fine turbidites. Below the 150–200 m, although a decrease in recovery, a stiffer hemipelagic mud seems to be the prevailing sediment. The recovered sediments from the site U1399 show a more hemipelagic composition with some fine-grained turbidites and very thin ash layers that increase their percentage with depth. The distal-most site U1398 shows a higher volcanoclastic composition mainly in the upper ca. 50 m. In depth, the presence of hemipelagic sediments increase up to 200 m, where below this depth is the prevailing sediment. Bathymetric and seismic data (Figures 1 and 2) show a channel system that may drain submarine sediments from Dominique towards the south. Based on these observations and data extracted from previous studies (Boudon et al., 2007; Le Friant et al., 2002), we interpret that the volcanoclastic sediments present in the area of the hole U1398 have their origin in Dominica rather than Martinique.

4.2 | Geotechnical properties of the Grenada Basin sediments

The measured initial (in situ) void ratio of the 19 whole-round samples varies between 1.4 and 2.8 (Figure S3). Sediment compressibilities derived from the slope of the virgin consolidation line (C_c) vary between 0.31 and 1.42 (Table 2). The use of logarithmic regression of the virgin consolidation line for each sediment sample allows us to calculate the geotechnical parameters at deposition (σ'=1 kPa) (Figure 3). Initial values are used hereinafter as depositional values. Thus, initial porosity (ϕ_0), hydraulic conductivity (k_0) and specific storage (Ss_0) refer to their depositional values. Initial porosity varies between 0.71 and 0.88, and initial specific storage between 0.001 and 0.008 m^{-1} (Table 2). In general, initial hydraulic conductivities (k_0) are low ($10^{-9.3}$–$10^{-8.1}$ m/s) (Table 2). There is no straight forward correlation between geotechnical parameters. Hence, the higher the initial porosities, the higher

TABLE 2 Hydromechanical properties from oedometer tests, grain size analysis and down hole logs

Hole	Section	Depth (mbsf)	Clay(%)	Silt (%)	Sand (%)	C_c	ϕ_0	Ss_0 (m^{-1})	k_0 (m/s)	Pc	ORC	Mag. Susc. (SI 10^{-5})	NGR (counts)	Sample Q
1397B[a,b]	3H2	18.66	4.4	49.1	46.5	0.41	0.72	0.002	6.30E-10	125	0.9	820	17	0.04
1398B	7H1	42.88	12.8	56.4	30.8	1.24	0.87	0.005	—	338	1.0	215	10	0.01
1398B[a,b]	9H4	62.7	12.2	67	20.7	0.89	0.82	0.006	2.70E-09	453	1.0	1565	12	0.03
1398B	18H7	136	10.1	45.4	44.5	1.42	0.87	0.007	—	735	0.9	953	12	0.01
1399B[b]	1H3	4.21	12.9	54.9	32.2	0.84	0.81	0.007	2.84E-09	24	0.9	1,112	13	0.02
1399B[b]	4H4	30.55	13.7	75.8	10.5	0.69	0.78	0.003	1.55E-09	149	0.8	301	14	0.03
1399B[b]	6H3	46.54	20.1	76.1	3.9	0.75	0.79	0.005	1.32E-09	202	0.8	198	33	0.03
1399B[b]	13H1	102.7	13.3	51.5	35.2	0.87	0.81	0.007	2.61E-09	395	0.6	1,486	12	0.02
1399B[b]	19H3	138.9	11.1	83.1	5.8	0.67	0.77	0.004	1.41E-09	670	0.8	105	19	0.04
1399B[b]	24H2	162.2	6.1	37.2	56.7	0.43	0.73	0.003	—	865	0.8	717	13	0.04
1399B[b]	27H2	176.1	10.2	52.2	37.5	0.71	0.79	0.006	—	1,059	0.8	599	22	0.04
1400C	3H4	27.21	8.8	55.8	35.5	1.39	0.88	0.004	—	397	1.6	235	11	0.01
1400C	5H6	47	23.6	48.9	27.5	0.68	0.81	0.007	6.57E-09	400	1.4	252	29	0.06
1400C	7H2	61	23	59.1	17.9	1.07	0.84	0.006	7.34E-10	505	1.1	175	21	0.07
1400C[b]	10H4	84	35.6	36.7	27.7	0.31	0.71	0.001	4.79E-10	230	0.4	156	27	0.03
1400C	13H4	109	11	28.6	60.4	1.33	0.85	0.007	4.62E-09	592	0.7	232	11	0.05
1400C[b]	19H4	159	24.6	42.9	32.5	0.35	0.71	0.001	—	811	0.7	498	24	0.04

Abbreviations: C_c, compressibility; k_0, initial hydraulic conductivity; OCR, over consolidation ratio; Pc, preconsolidation pressure; Sample Q, minimum sample quality (<0.04 Very good, 0.04–0.07 good to fair) (Lunne et al. (2006); Ss_0, initial specific storage; ϕ_0, initial porosity.

[a]Mean values of two tests.

[b]Sample results used for sediment characterization. Initial values are referred at deposition ($\sigma' = 1$ kPa).

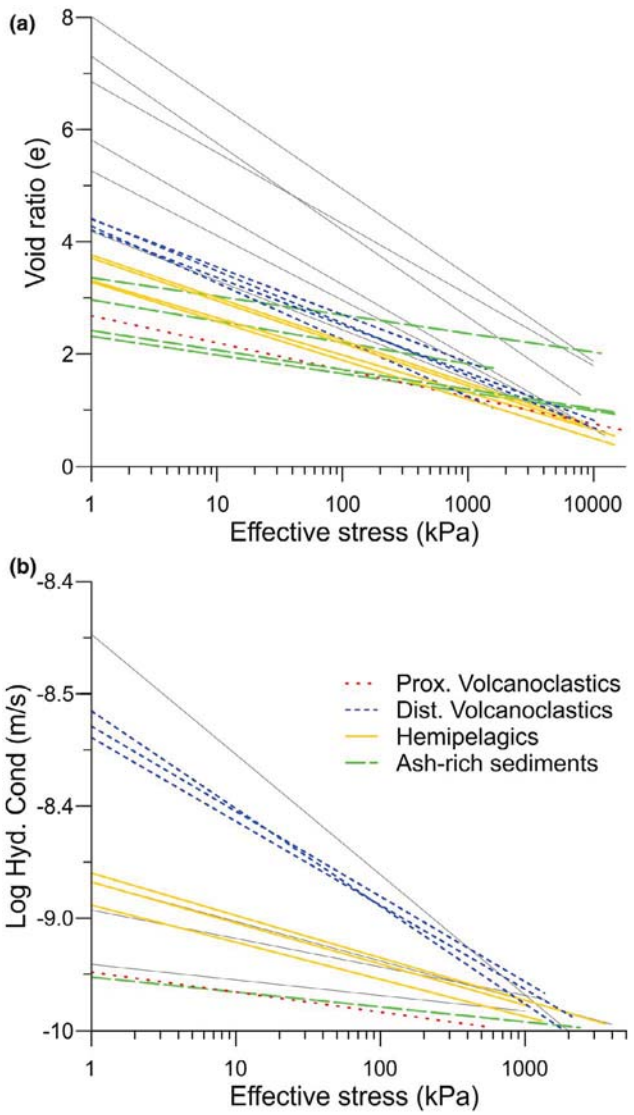

FIGURE 3 Extrapolation to 1 kPa of the slope of the virgin consolidation line for a) consolidation and b) permeability tests results. Grey lines correspond to samples not selected for sediment physical properties characterization. See Figure S3 for the consolidation curve results

the compressibility and initial specific storage. Some sample results have been discarded for the modelling as the samples show: (a) samples with extreme values (e.g. $C_c > 1.2$ in samples 1398B-7H1, 1398B-18H7 and 1400C-3H4) (Table 1) which could be related to structuring issues, or (b) poor quality control during consolidation tests ($Q > 0.04$ in samples 1400C-5H6, 1400C-7H2 and 1400C-13H4) as defined in Lunne et al. (2006) (Table 2).

To distinguish the different sediment types that will be set in basin, we used the regression line of the virgin consolidation curves (Figure 3). These regression lines show two main sediment groups with significantly different C_c (Figure 3a): one group with compression indices between 0.3 and 0.45 (green and red) and another between 0.67 and 0.9 (blue and yellow) (Figures 3 and 4). In terms of permeability, we can distinguish three groups of samples (blue and yellow; green; red) based on their permeability behaviour with respect to effective stress (Figure 3b). The samples displaying further reduction in hydraulic conductivity with increasing effective stress (blue lines in Figure 3b) are those displaying higher compressibility (Figure 4).

The relationships among initial porosity, initial specific storage and compressibility have been used together with the consolidation and permeability test results as a tool to unveil four sediment clusters (Figure 4). The samples 1400C-10H4 and 1400C-19H4 show low compressibility values, low initial porosity, low specific storage and a balanced granulometrical composition (Table 1, red colour in Figures 3 and 4). According to diffraction results carried on samples 1400C-10H4 and 1400C-19H4, they correspond to ash-rich sediments (personal communication, Lafuerza 2020). Thus, these ash-rich sediments have a mean initial porosity values of ca. 0.71, specific storage ca. 0.001 m^{-1} and hydraulic conductivity ca. $10^{-9.3}$ m/s (Table 3). To the contrary, the other samples could be divided into clayey-silt or sandy-silt sediments. In the opposite side is the group of samples with higher compressibility, initial porosity and specific storage (blue dots in Figure 4). Their initial values are ϕ_0 ca. 0.81, Ss_0 ca. 0.007 m^{-1} and k_0 ca. $10^{-8.5}$ m/s (Table 3). These sediments, composed by samples 1398B-9H4, 1399B-1H3 and 1399B-13H1, are sandy-silt with a mean clay content <13% showing the higher mean magnetical susceptibility of 1565 SI 10^{-5} (Table 2 and Figure S2) and correspond to high-compressibility distal volcanoclastics. The other two sediment clusters show rather more intermediate values. The sediments from samples 1399B-4H4, 1399B-6H3, 1399B-19H3 and 1399B-27H2 are clearly clayey silt (mean clay content >13%) with mean values of ϕ_0 ca. 0.78, Ss_0 ca. 0.005 m^{-1} and k_0 ca. $10^{-8.8}$ m/s; and correspond to hemipelagic sediments (Table 3 and yellow colour in Figures 3 and 4). Contrary, the sediments from samples 1397B-3H2 and 1399B-24H2 are sandy-silt (Table 3 and green colour in Figures 3 and 4) with mean values of ϕ_0 ca. 0.73, Ss_0 ca. 0.003 m^{-1} and k_0 ca. $10^{-9.2}$ m/s, and correspond to low-compressibility proximal volcanoclastics. Hereinafter, the two volcanoclastics sediments types will be named as distal and proximal volcanoclastics.

4.3 | Hydrogeological evolution of the Grenada Basin

On the basis of stratigraphic architecture, sedimentary facies and hydromechanical properties, basin hydrogeological modelling has been carried out. Model results presented in this section do not account for the emplacement of the debris avalanches related to the Montagne Pelée flank collapses, and is meant to use as a base model to elucidate the effect of

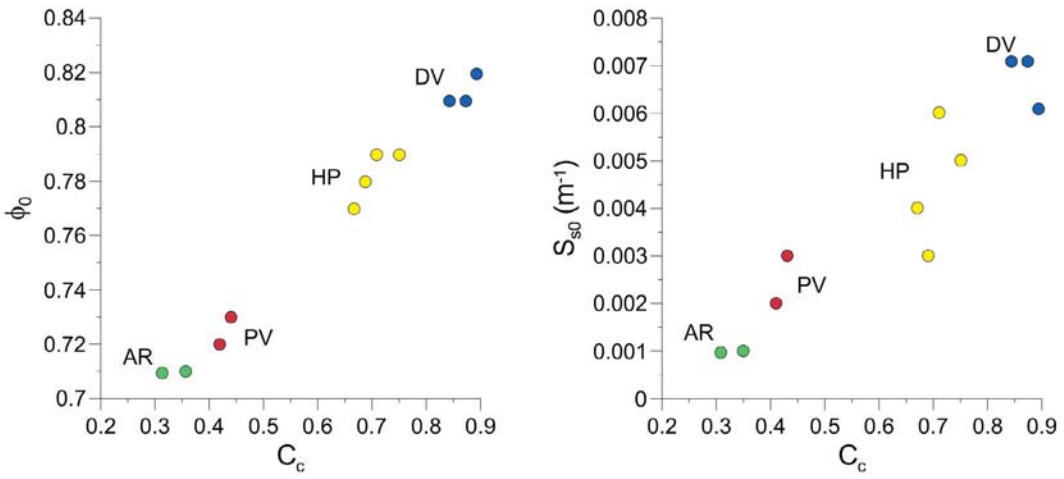

FIGURE 4 Sediment classification according to the geotechnical properties derived from oedometer tests. HP, hemipelagic sediments (yellow); PV, proximal volcanoclastics (red): DV, distal volcanoclastics (blue); and AR, ash-rich sediments (green) (Table 3). C_c, compressibility; ϕ_0, initial porosity; S_{s0}, initial specific storage

TABLE 3 Design initial ($\sigma' = 1$ kPa) hydromechanical properties used as input for the numerical modelling

	G_s (g/cm^3)	C_c	ϕ_0	Ss_0 (m^{-1})	k_0 (m/s)
Proximal volcanoclastics	2,750	0.42	0.73	0.003	$10^{-9.2}$
Hemipelagics	2,650	0.70	0.78	0.005	$10^{-8.8}$
Ash-rich sediments	2,760	0.31	0.71	0.001	$10^{-9.3}$
Distal volcanoclastics	2,750	0.86	0.81	0.007	$10^{-8.5}$

Abbreviations: C_c, compressibility; G_s, Grain density; k_0, initial hydraulic conductivity; Ss_0, initial specific storage;ϕ_0, initial porosity.

emplacement of the debris avalanches in the Grenada basin. Model results show that sediment physical characteristics at deposition (ϕ_0, S_{s0} and K_0) have a major effect in the subsequent evolution of porosity and permeability as a result of overburden development. The model outcome for the Present-day margin (no accounting for the debris avalanche emplacement) shows that porosities decrease with depth throughout the model and values above 0.65 are present only at shallow depths (<200 mbsf) (Figure 5a). Although in most of the model the porosity gradient is ca. 0.08 m^{-1}, in the distal part of the modelled profile this gradient is ca. 0.6 m^{-1} in the upper ca. 200 mbsf and then increases rapidly to ca. 0.9 m^{-1} in the depth range between 200 and 300 mbsf decreasing again to a lower constant value of ca. 0.15 m^{-1}. However, some layering is depicted in the central and proximal part of the model. This layering results from the alternation of layers primarily composed of proximal volcanoclastic and ash-rich sediments, and others with a more hemipelagic composition. The higher compressibility of the hemipelagic sediments results in lower porosities when buried at depth, despite their higher initial porosity (Table 3). This effect is hindered in the hydraulic conductivity model except in the deepest part of the basin where it can be clearly seen (Figure 5b). In the deepest-central part, hydraulic conductivities decrease up to 10^{-11} m/s, whereas in most of the margin values vary between $10^{-9.5}$ and $10^{-10.2}$ m/s (Figure 5b). Only in the shallowest ca. 100 mbsf values higher than $10^{-9.2}$ m/s are recorded. In the distal (western) part of the model, where distal volcanoclastics prevail, the higher hydraulic conductivities (>10^{-9} m/s) are restricted to the first ca. 100 mbsf. This interval also corresponds to the lowest porosity gradient in the model (Figure 5a).

The fluid flow patterns in most of the margin are vertical or quasi-vertical (Figure 5c). Deviations from the vertical flow are controlled by location of depocenter (where the higher velocities ca. 3 cm/kyr occur) and stratigraphic arrangement (Figure 5c). Along the slope (up to km ca. 24), fluid flow develops outward from the margin due to the inclined basement and bathymetry. Excess pore pressures reaches 22 MPa in the central part of the model coinciding with location of the main depocenter (Figure 5c); it reaches ca. 10 MPa in the upper slope, where the sedimentary load is lower, and it is <7.3 MPa in the distal area, at the base of the model (ca. 3.5 km depth). Also, in this area, the fluid flow velocities are below 0.5 cm/kyr. Finally, overpressure ratios (λ^*) in the entire model at Present day are very low (Figure 5d)

COLOUR online, B&W in print

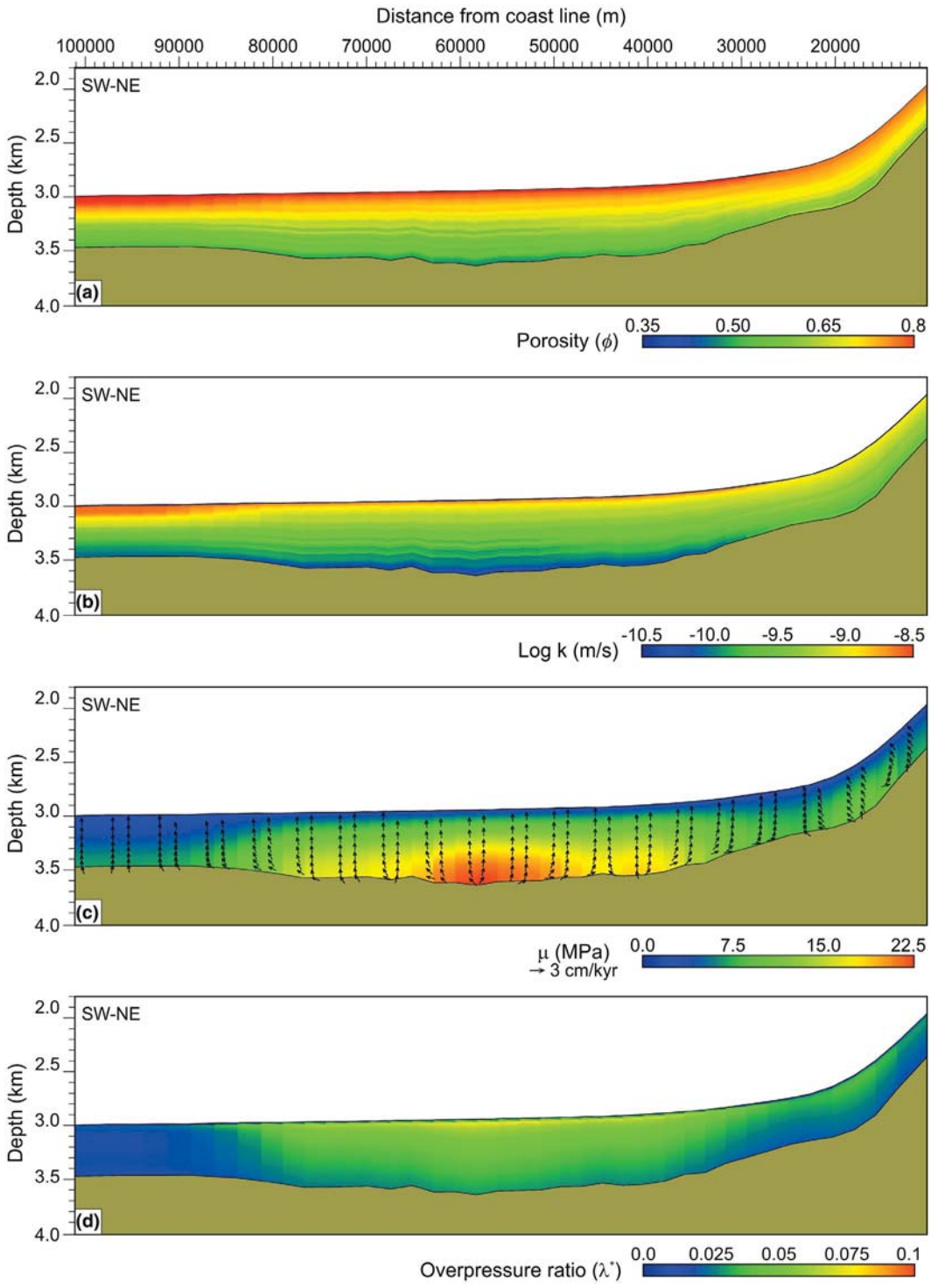

FIGURE 5 (a) Output of BASIN simulation at Present day for the Grenada Basin (not accounting for deposition of the debris avalanches): (a) fractional porosity, (b) log hydraulic conductivity (m/s), (c) Excess pore pressure (MPa) and d) Overpressure ratio (λ^*). Vertical exaggeration 12:1. See Figure 1 for profile location

with values ranging 0–0.093. The maximum λ^* are below 0.1 (i.e. excess pore pressure is 10% of the total stress minus hydrostatic pressure) and are mainly located in the central part of the model with values higher than 0.05 above 250 mbsf (Figure 5d). In addition, values above λ^* ca. 0.06 are shown in the first tens of meters of the upper slope.

To ground truth the model results, the Present-day sea floor of this model (not accounting for the DADs emplacements) can be compared with the interpolated sea floor outside the DADs and SLD location (Figure 6). The maximum error found between the model results and the Present-day sea floor is around 1.1% of the sedimentary column (Figure 6d).

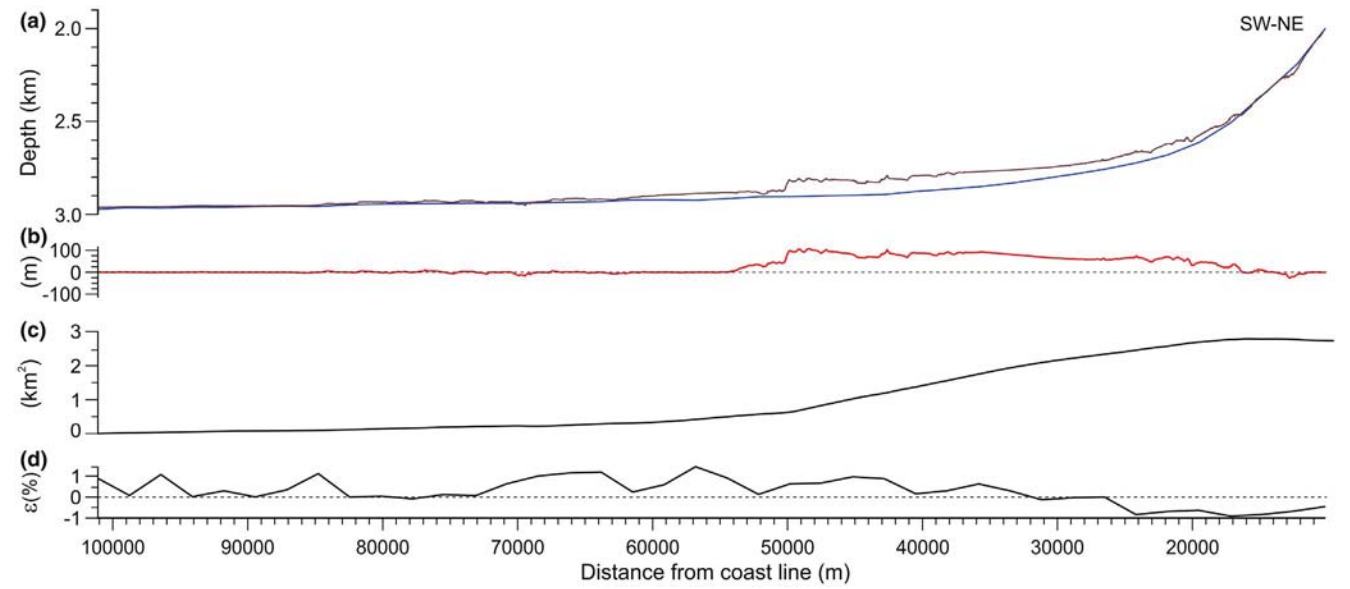

FIGURE 6 (a) Sea floor along CARA-16 profile: real (brown line) and Present-day BASIN model result (blue line) not accounting for avalanche emplacement; (b) Difference between the two profiles in a); (c) Cumulative profiles difference from (b); (d) Sea-floor Present-day model error (per cent) normalized by the thickness of the sedimentary column

This very low error ensures that the sediment type distribution and the sedimentary architecture used in the model are robust enough.

4.4 | Effect of debris avalanches emplacement on pre-existing sediments

The effect of the emplacement of the submarine debris avalanches DAD1 to DAD3 on the margin hydrogeology has been investigated. The Present-day sea-floor morphology of the study area clearly shows hummocky-like features on top of the debris avalanches lobes (Figures 1 and 6). The difference between the Present-day sea floor and that of the sea floor interpolated from data outside the area affected by the DADs is considered as the contribution to the overburden by emplacement of the debris avalanches along profile CARA-16 (Figure 6b). Their cumulative unit volume along the profile CARA-16 is 2.76 km^3 and is used herein after as the amount of volcanoclastic material that was deposited during occurrence of the DADs (Figure 6c). According to the volumes of the on-land three flank collapses and the relationship between the on-land volume of the third flank collapse and the volume of the DAD3, the unit volume of the debris avalanches DAD1 + DAD2 are split as DAD1 = 1.65 km^3, DAD2 = 0.87 km^3 (DAD1 + DAD2 = 2.52 km^3) and ca. 0.2 km^3 for DAD3. The submarine debris avalanches are considered to be composed not only of previous deposited sediments in the upper slope, but also of volcanic blocks especially in the more proximal area of the DAD's. Hence, due to the lack of proper input data and the unavailability to add a fifth sediment type to the model, the sediment composition of the avalanches has been tentatively set based on the sediment type abundance in the first 100 m of the core U1397B. Thus, a ca. 92% corresponds to proximal volcanoclastics, ca. 7% hemipelagics and 1% to ash-rich sediments. The thicknesses of these sediments corresponding to the avalanches have been decompacted by using van Hinte's equation to tentatively reproduce the ulterior compaction that can be observed at Present day. By using this approach, a density of ca. 2050 kg/m^3 prior to their emplacement has been obtained, which is in agreement with the density of ca. 2000 kg/m^3 suggested by Brunet et al. (2017). The run-out distance of DAD1 + DAD2 has been set to a maximum of 41 km from the coastline. This assumption is in accordance with the lack of DAD material at IODP site U1400 that is located at 43 km off the coastline (Brunet et al., 2016). However, it is in contradiction with previous authors (e.g. Le Friant et al., 2015) who set the limit of the DAD1 + DAD2 beyond the site U1400. The distribution of DAD1 + DAD2 unit volume along the profile has been set following the parabolic shape of DAD3. The model also accounts for the background sedimentation in between emplacement of the DAD1 + DAD2 and DAD3.

Emplacement of DAD1 + DAD2 at 127 ka had a major impact on the stress state of the margin, as the overpressure ratio reached values ca. 0.98 in the central part of the DAD emplacement area (Figure 7a), i.e. the pore pressure was close to lithostatic implying that the pre-existing sediments could easily liquefy or glide given a minimum slope gradient. Such significant increase in overpressure is recorded in the model up to 41km off the coast line, no overpressure ratios are recorded beyond the emplacement of the

COLOUR online, B&W in print

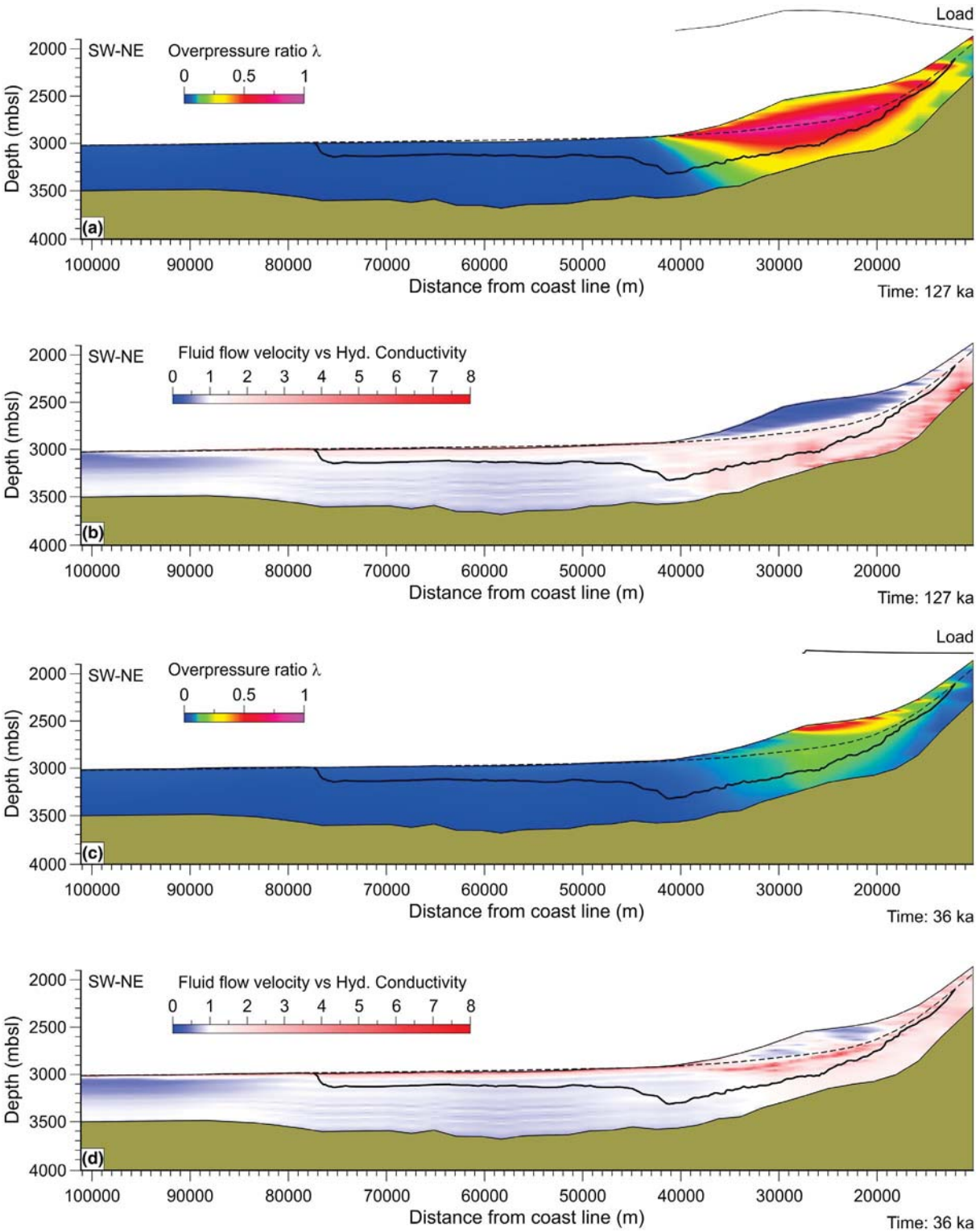

FIGURE 7 Overpressure ratios due to the emplacement of the debris avalanches: (a) DAD1 + DAD2 at 127 ka; (c) DAD3 at 36 ka. The amount and extension of debris avalanche load are depicted. Calculated ratio of fluid flow velocity to hydraulic conductivity: (b) emplacement of the debris avalanches DAD1 + DAD2 at 127 ka; (d) emplacement of the debris avalanche DAD3 at 36 ka. Values below 1 mean hydraulic conductivity higher than fluid flow velocity; values larger than 1 mean fluid flow velocity is higher than hydraulic conductivity. Black line depicts the base of the deformed sediments. Dashed line depicts the sea floor from the model without debris avalanches emplacements (see Figure 5)

DADs. High overpressure ratio values occur even at depths higher than 300 mbsf below the DAD emplacement area. The depth at which overpressure ratio of ca. 0.75 is reached coincides well with the base of the deformed sediments in the more proximal area (11–24 km from the coast line) and therefore could be considered that a minimum overpressure ratio of 0.75 is needed to cause the high sediment deformation observed. As expected from its lower volume (1.8 km3), overpressures impact of DAD3 emplacement on pre-existing sediments is rather low (Figure 7c). Despite λ^* values of up to 0.24 develop at the base of the easternmost part of the model (Figure 7c), in this case, overpressure ratios higher than 0.7 are restricted to the first tens of metres of sediments right below DAD3.

Here, we analyse qualitatively the fluid flow as the ratio of the fluid flow velocity (q) versus the hydraulic conductivity (k) of the sediments although values are reported for a better understanding. Thus, a $q/k > 0$ means that the derived fluid flow is higher than the hydraulic conductivity of the sediments; $q/k < 0$ means that hydraulic conductivities are higher than the fluid flow. In other words, when $q/k > 0$ not all the fluid can flow through the sediments. The derived fluid flow velocities at least 2.5 times higher than the sediment hydraulic conductivities (reddish colours in Figure 7b,d) are found in the area of deformed sediments. This effect is also shown in the thin deformed sediment layer that develops up to 77 km from the coast line. Nevertheless, the higher fluid flow velocities are located in the sedimentary column below DADs emplacement area, where values up to 7.2 times the hydraulic conductivity reach the base of the model (Figure 7b). Again, the lower load induced by the DAD3 resulted in lower fluid flow velocities (Figure 7d). This model also shows that, at depth, the variable hydraulic conductivities of the different materials is displayed as bands in the fluid flow velocity field.

Temporal evolution of overpressures at selected locations on the profile show that before flank collapses (11.2 Ma–127 ka), overpressure ratios were below 0.1 in the entire model (Figure 8). At the time of emplacement of the DAD1 + DAD2 (127 ka), the overpressures rose sharply up to 0.98. In the central area where the DADs emplaced (synthetic well at 26 km), the overpressure ratios are higher and affect a thickest package of sediments; values higher than 0.7 reach up to 200 m below the DADs materials (Figure 8b). The most proximal synthetic well (at 16 km) show a shallower influence of overpressures build up due to the emplacement of the DADs with maximum values $\lambda^* > 0.7$ (Figure 8a). In the most distal synthetic well, located at 36 km in the profile (Figure 2), overpressure ratios higher than 0.2 develop above 300 mbsf,

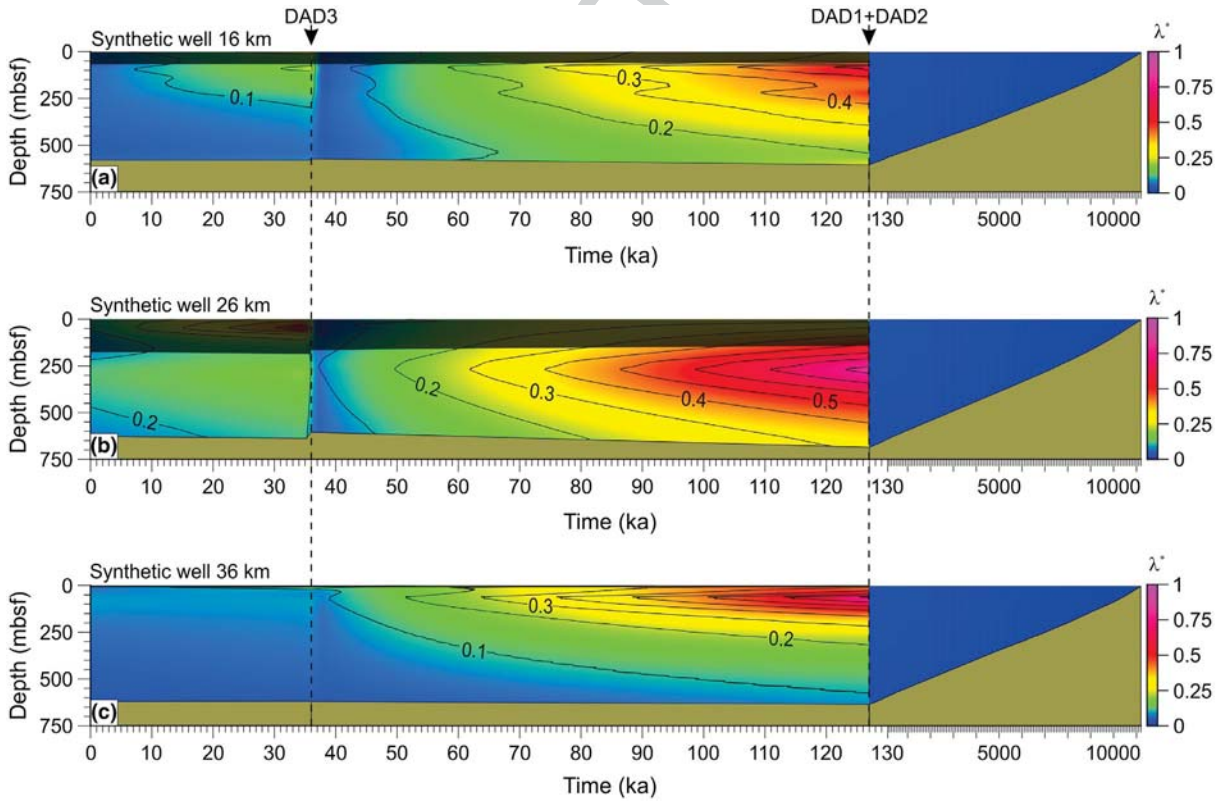

FIGURE 8 Model evolution through time at the synthetic wells location: (a) 16 km, (b) 26 km and (c) 36 km. Emplacement of the debris avalanches DAD1 + DAD2 and DAD3 are depicted. Note the different time scale from 11.2 Ma to 127 ka (to the right) with respect to 127 ka to Present day (to the left). See Figure 2 for sites location. Grey masking box depicts the avalanches thickness; its base corresponds to the sea floor prior to the avalanches

which indicates that the emplacement of DAD1 + DAD2 on pre-existing sediments had major hydrogeological effects far beyond its depositional area. After the emplacement of DADs, these overpressures dissipated through time at a rate of ca. 0.01 kyr^{-1} in the uppermost 100 mbsf, evolving from $\lambda^* > 0.8$ to less than 0.1 before 36 ka (Figure 8c). A similar decrease occurred at the synthetic wells located at 16 km and 26 km (Figure 8a,b), although such a decrease is not only restricted to the shallowest sediments but affects the entire sedimentary column. The emplacement of DAD3 had no appreciable effect at the synthetic well at 36 km, whereas in the proximal area λ^* reached values up to 0.35 and dissipated more slowly (ca. 0.003 kyr^{-1}) than the ones generated by DAD1 + DAD2. Only in the sediments immediately below DAD3, λ^* reached values up to 0.74 (Figure 8a). A relevant point is that overpressure ratios above 0.2 have been maintained through time reaching depths of 200 to 500 mbsf until Present day.

Fluid flow velocities related to the emplacement of the DAD's as observed at the synthetic wells show that the highest velocities occur deeper in the sedimentary column when moving to more westward distal positions (Figure 9). Thus, from synthetic well at 16 km (Figure 9a) to the one at 36 km (Figure 9c) the maximum fluid flow velocities move from 200 mbsf to 550 mbsf. These depths match the base of the deformed and remobilized sediments (Figure 7), where the maximum fluid flow velocities developed with values of 8 to 12 m/kyr. Such high velocities remain through time around the central synthetic well (Figure 9b).

5 | INTERPRETATION AND DISCUSSION

5.1 | Controls on sediment deformation

The marine sediments west off Montagne Pelée record the emplacement of up to 300 km^3 submarine landslide deposits resulting from three subaerial volcanic flank collapses (Figure 1) (Brunet et al., 2016). Prior to the occurrence of the first flank collapse, the Grenada Basin sediments consist of stacked turbidites, ash-rich layers and hemipelagic sediments with a mean sedimentation rate of 5–10 cm/kyr (Reid et al., 1996). These sedimentation rates (loading rate) in combination with the sediment hydraulic and compressibility characteristics result in the development of little overpressure in the Grenada Basin (Figure 5d). Previous works suggest that sea-floor sediment deformation shown in the seismic data results from the loading of the DADs onto the pre-existing sediments (e.g. Brunet et al., 2016; Le Friant

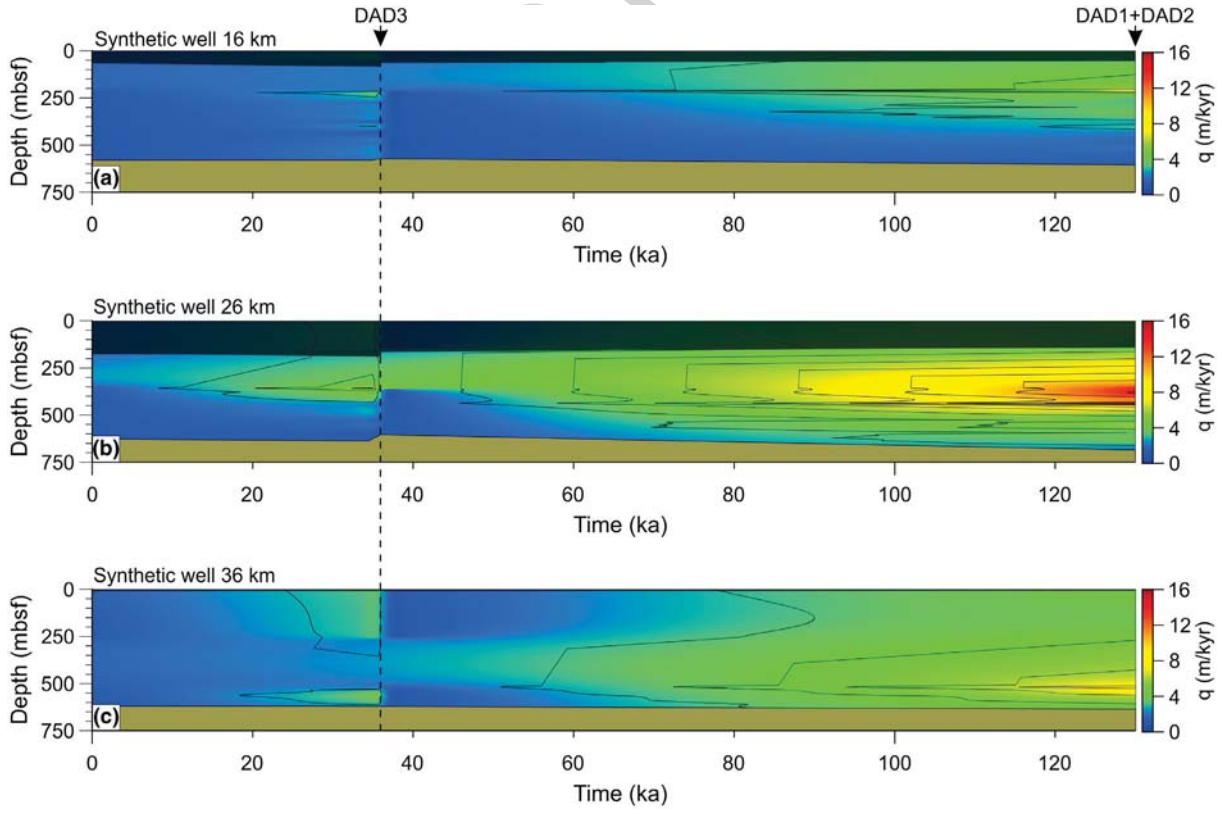

FIGURE 9 Evolution of fluid flow velocities due to emplacement of the debris avalanches at the synthetic wells location: (a) 16 km, (b) 26 km and (c) 36 km. Grey masking box depicts avalanche thickness; its base corresponds to the sea floor previous to the avalanches. See Figure 2 for synthetic wells location

et al., 2003, 2015). Despite the fact that the volume of the subaerial collapsed material is well known from on-land observations (e.g. Boudon et al., 2007), the total volume involved in the submarine debris avalanches is not well constrained. Indeed, during motion of the debris avalanches, they may eroded and/or incorporated pre-existing sediments while losing material along their path. Because of this, we calculate the volume of the submarine debris avalanches from the seafloor geomorphology. This method seems the best approximation due to the lack of better constraints. Emplacements of the debris avalanches triggered a sharp increase of overpressures in the previous sediments (Figure 7). As expected, the larger the size of the debris avalanche, the higher the resulting overpressures and the area over which the overpressures increase. The model shows that the areas with high overpressure occur where the highest sediment deformation has been identified in the IODP-340 cores and acoustic dataset (Le Friant et al., 2015). The model depicts that the depths at which mid- to high-overpressure ratios ($\lambda^* > 0.5$) are reached in the proximal area coincide with the base of the deformed sediments. Thus, it seems that such overpressure ratio is sufficient to overcome the undrained peak shear strength of the sediment in the proximal region (Figures 7 and 8).

In the area surrounding site U1400 (see Figure 4), the combination of high overpressures and low overburden could favour the formation of thrust structures (Figure 2) due to the emplacement of DAD1 + DAD2 (Brunet et al., 2016). The over consolidation ratios (OCR)ca. 1.5 of the sediments tested from the core 1400C at depth between 40 and 85 m could be explained by an exhumation of ca. 40 m (Table 2). However, deeper samples in the same site are underconsolidated (OCR ca. 0.6) indicating that excess pore pressures exist at Present day (λ^* ca. 0.3–0.4). However, these laboratory-based values are slightly higher than the model results (λ^* ca. 0.2–0.3) (Figure 7). Hence, higher overpressures could develop beyond the debris avalanche emplacement, or overpressures did not decrease through time as fast as shown in the model results (Figure 7). The higher compressibility of hemipelagic sediments may evolve in low permeability layers that could hinder the long-term fluid release from the more permeable volcanoclastic layers. As stated by Puzrin et al. (2016), this effect could contribute to a strain softening favouring a shear band propagation and a further sediment mobilization. Nonetheless, these fluid pressure mechanisms might not create the observed deformation and thrust structures alone without accounting for the debris avalanche material weight that pushed the pre-existing sediments. This type of sediment deformation creating fold and thrust structures and distal deformation, even 30 km away from the source, bear resemblance with observed sediment structures observed in frontal moraines due to a glacier pushing during long periods (Ingólfsson et al., 2016). We, therefore, infer that the sediment deformation identified west off Martinique did not occur instantaneously, but evolved through time after emplacement of the DADs, which is in agreement with Hornbach et al. (2015). It is also supported by the model (Figure 8) that shows the persistence of low to mid overpressure through time that could maintain the sediment deformation between the emplacement of DAD1 + DAD2 and DAD3. Even the low effect on overpressure built up due to the emplacement of DAD3 compared to the previous DADs, it may be key to maintain the long term sediment deformation.

5.2 | Model uncertainty derived from input physical properties

Modelling is prone to potential sources of output uncertainty. Parameter uncertainties are related to the models architecture and variability in mechanical and hydraulic properties. The first incorporates seismic data resolution issues, choice of relationship for time to depth conversion, accuracy of sound speed determination and uncertainties in facies attribution (together with heterogeneity) along the modelled transect (Llopart et al., 2019; Nadim, 2015). Another source of uncertainty is related to the timing of occurrence of the flank collapses since accurate ages could not be constrained for DAD1 and DAD2, but also proper to the dating techniques used. Basin analysis models are commonly developed with the best available data to construct one deterministic geological model. Thus, uncertainties resulting from the model structure are thus hard to evaluate. Potential ways to estimate these uncertainties are reviewed in Nilsson et al. (2007) and are beyond the scope of the present study. With regard to the variability in mechanical and hydraulic properties, Monte Carlo analysis provides a way to assess their influence on output uncertainty (in this case overpressure ratio).

When models are made of independent variables, the ideal approach would be to test the influence of the different geotechnical parameters used in the simulation one at a time. Such approach is, however, not adequate here as the porosity, permeability and compressibility/specific storage are interdependent parameters. Indeed, a decrease in the porosity has to be also associated with a decrease in the other two parameters, and vice versa (Figure 3). Thus, when porosity is increased, permeability and specific storage need to be increased as well, following the consolidation curves derived from the geotechnical tests. A set of confidence intervals (CI) for each sediment type and geotechnical property (Table 4) are used as inputs for the Monte Carlo analysis. The set of initial parameters created for Monte Carlo analysis have been obtained by using a Simple Random Sampling (SRS) within the CI with a confidence level of 98% (Hurtado & Barbat, 1998). Hence, we computed a total of 512 models by randomly creating a series of parameter sets. The results of overpressure ratio from all the models have been averaged and we calculated the standard deviation to the reference

TABLE 4 Parameters derived from geotechnical tests in this study, mean values (μ), standard deviation (σ) and confidence interval (CI), for each physical property and sediment type, for a confidence level of 98%

	Proximal volcanoclastics		Distal volcanoclastics			Hemipelagics				Ash-rich sediments	
	1397B 3H2	1399B 24H2	1398B 9H4	1399B 1H3	1399B 13H1	1399B 4H4	1399B 6H3	1399B 19H3	1399B 27H2	1400C 10H4	1400C 19H4
ϕ_0	0.72	0.73	0.82	0.81	0.81	0.78	0.79	0.77	0.79	0.71	0.71
μ	0.725		0.81			0.78				0.70	
σ	0.007		0.0057			0.009				0.003	
C_i	0.71 to 0.74		0.80 to 0.83			0.76 to 0.80				0.70 to 0.72	
$log\ k_0$ (m/s)	−9.2	—	−8.57	−8.55	−8.58	−8.81	−8.88	−8.85	—	−9.32	—
μ	−9.2		−8.56			−8.84				−9.32	
σ	0.035		0.015			0.035				0.035	
C_i	−9.28 to −9.12		−8.60 to −8.53			−8.93 to −8.77				−9.40 to −9.24	
S_0 (m^{-1})	0.003	0.002	0.006	0.007	0.007	0.003	0.005	0.004	0.006	0.0009	0.0008
μ	0.0025		0.0066			0.0045				0.0008	
σ	0.0007		0.0005			0.0012				0.00001	
C_i	0.001 to 0.004		0.005 to 0.008			0.001 to 0.008				0.001 to 0.001	

Note: Confidence interval has been used to generate the input data for the Monte Carlo analysis.

Abbreviations: ϕ_0, initial porosity at 1 kPa, k_0, decimal logarithm of initial hydraulic conductivity at ϕ_0, S_0, initial specific storage at ϕ_0.

COLOUR online, B&W in print

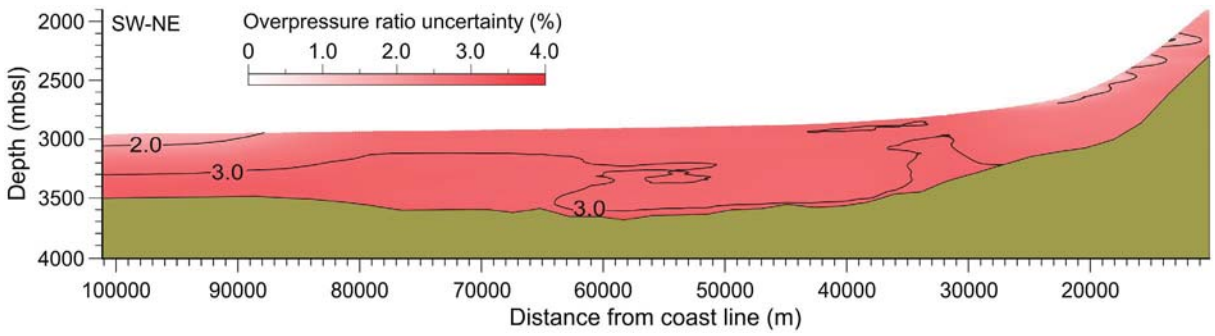

FIGURE 10 Uncertainty in overpressure ratio results derived from variability in mechanical and hydraulic properties using a Monte Carlo analysis over the BASIN model

COLOUR online, B&W in print

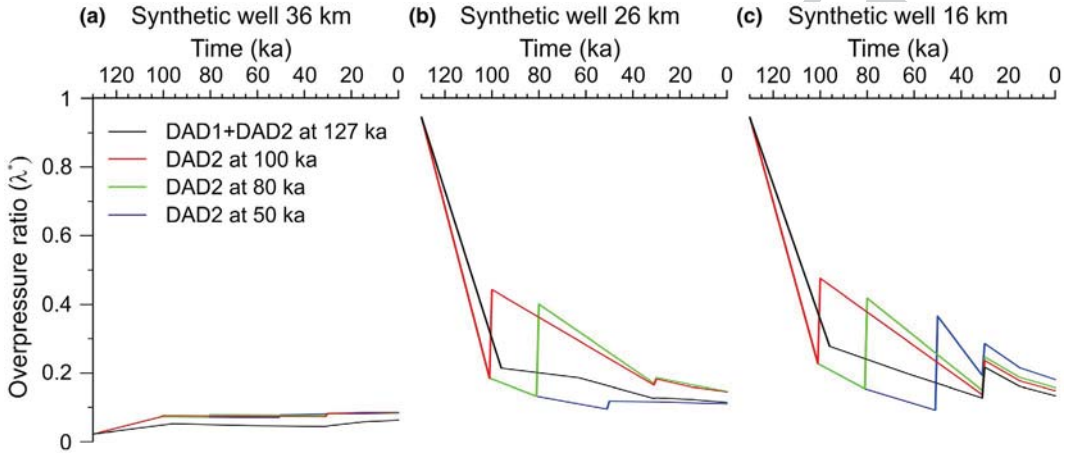

FIGURE 11 Overpressure ratio evolution at 100 mbsf with occurrence of debris avalanche DAD2 at different times at the three synthetic wells (see location in Figure 2). DAD1 is fixed at 127 ka, DAD3 at 36 ka while DAD2 varies: 127 ka (black), 100 ka (red), 80 ka (green) and 50 ka (blue)

model (Figures 5 and 10). The confidence interval for the hydraulic conductivity of proximal volcanoclastics and ash-rich sediments has been calculated using the maximum value of the standard deviation of the two other sediments (distal volcanoclastics and hemipelagics). This solution has been adopted because only one permeability test was available for each one of the proximal volcanoclastics and ash-rich sediments.

Given the available mechanical and hydraulic data, the output from the Monte Carlo simulation shows that the mean values of uncertainty in the whole model are below 4% (Figure 10). The maximum uncertainty, around 3.5%, occurs in the deeper parts in the centre of the model, where hemipelagic sediments are more common (Figure 4). The higher standard deviation of the initial porosity and hydraulic conductivity of hemipelagic sediments is reflected in these higher uncertainty values. Despite a larger number of oedometer tests, particularly with concurrent permeability evaluation, on ash-rich sediments and proximal volcanoclastics sediments, could ascertain whether this uncertainty is genuine, the uncertainty values are low. Thus, these results entrust the model outcomes.

5.3 | Timing of the flank collapses

As stated above, the timing for the three Montagne Pelée flank collapse events is still under debate. How the timing of the flank collapses may have influenced the development of overpressures has been investigated by changing the timing of occurrence of DAD1 + DAD2. We have tentatively set the following scenarios for the two first events DAD1 and DAD2: (a) DAD1 + DAD2 at 127 ka (reference model); (b) DAD1 127 ka and DAD2 100 ka; (c) DAD1 127 ka and DAD2 80 ka and (d) DAD1 127 ka and DAD2 50 ka. The third event DAD3 is fixed at 36 ka. Background sedimentation continues between the emplacement of the debris avalanches. The three synthetic wells at 16, 26 and 36 km are also used to visualize results (Figure 11).

The history of overpressure development is significantly affected in the areas where the debris avalanches directly impact. However, when comparing the outcomes at Present day between the four models, the lower values of overpressure ratio occur when accounting for the simultaneous

emplacement of the DAD1 and DAD2 (reference model). Although here the emplacement is considered to occur at the same time (127 ka), they could take place within a range of tens to hundreds of years. The model shows no difference in overpressure generation at 127 ka whether the first two debris avalanches occur at the same time or just the DAD1. So the amount of sediment involved in the DAD1 (unit volume of 1.65 km^3) is enough to develop overpressure ratios close to 1. In the central synthetic well, the lower λ^* do not only occur at Present day but also before the emplacement of DAD3 when the time span between the emplacement of DAD1 and DAD2 is the highest (77 kyrs) (Figure 11b). Thus, the longer the time between debris avalanches the less pore fluids remain in the sediments due to compaction. Hence, the deposition offshore of the next debris avalanche will have less effect on the overpressure development. However, the emplacement of

COLOUR online, B&W in print

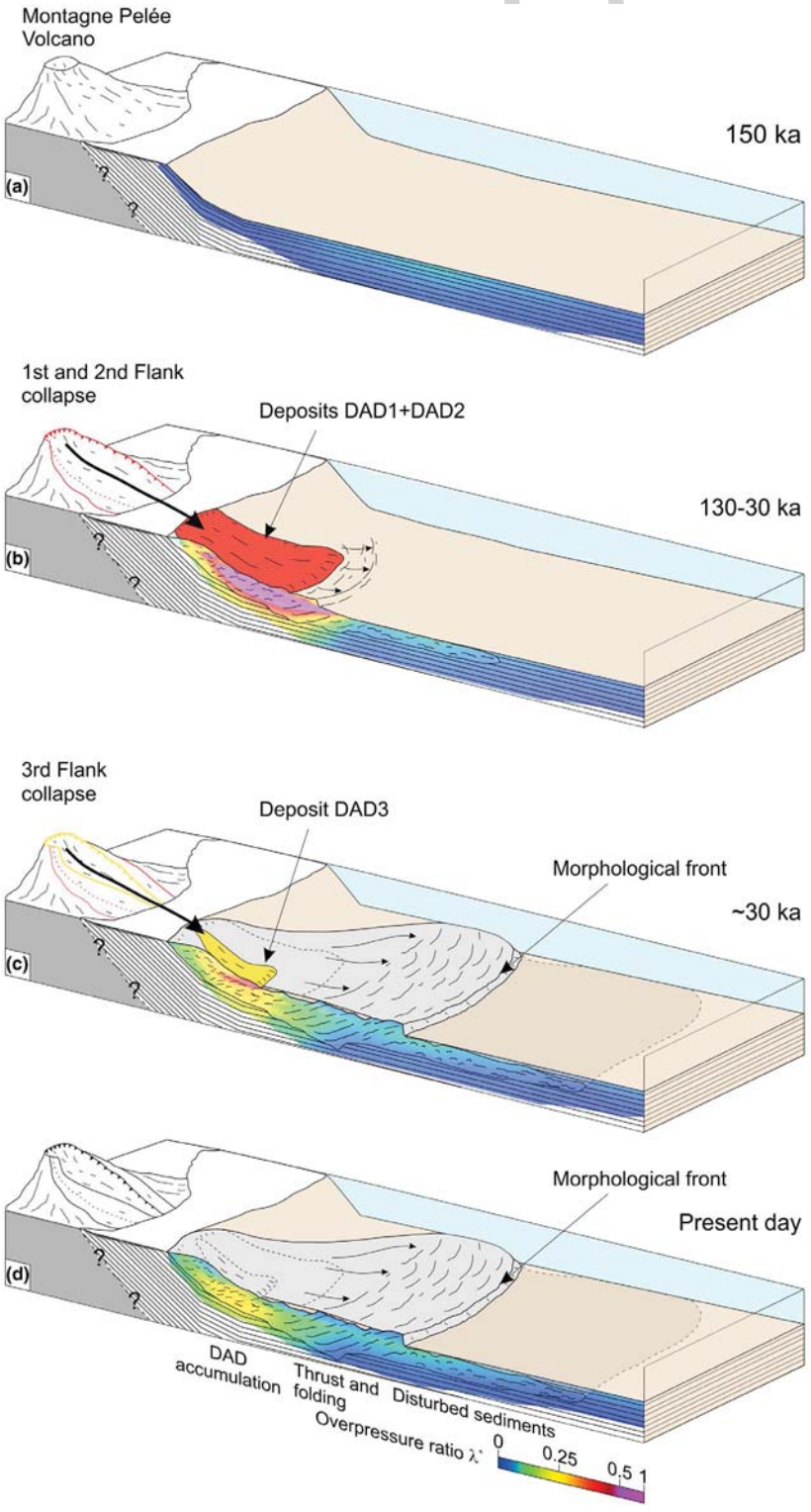

FIGURE 12 Conceptual model of the Grenada Basin evolution. (a) From Late Miocene to 127 ka low overpressure ratios developed; (b) The emplacement of the DAD1 and DAD2 triggered very high overpressure ratios and sediment deformation that persisted though time; (c) Emplacement of the DAD3 increased again the overpressures and contribute to the continuous sediment deformation; (d) Present-day overpressures are mid to low

DAD2 at 100 or 80 ka developed the same range of overpressures in the central well. To the contrary, in the most proximal area the longer the time in between events the higher the overpressure generated (Figure 11c). This difference between the most proximal and the central well could attain to the amount of load of the debris avalanches in between the two well locations. The lower load in the most proximal area is not enough to compact the sedimentary column at the same rate than in the central well; so if the DAD2 occurred at 50 ka, the proximal sediments still held enough pore fluid to develop mid overpressures. However, it is worth to point out that the occurrence in two separate events of the DAD1 and DAD2 favour sustained higher values through time that could favour the continuous sediment deformation. These sustained overpressures may act as a preconditioning factor for the sediments to fail especially in an area affected by a recursive earthquake loading. This analysis does not allow to establish the age of emplacement of the DAD2, but suggests that most probably DAD1 and DAD2 emplaced in separate events with 30 to 50 kyrs in between them. In turn, coupled fluid flow-deformation models accounting with strength parameters of the sediments will allow to verify the here proposed strain softening due to the combination of the DADS loading and the high fluid flow velocities.

6 | CONCLUSIONS

The marine sediments of the Grenada Basin, west off Martinique, have been affected by the emplacement of three flank collapse events during the last 127 kyrs. From geotechnical test carried out on samples from IODP-340 Expedition cores, four types of sediments have been identified with distinctive mechanical and hydraulic properties: proximal volcanoclastics, distal volcanoclastics, hemipelagic and ash-rich sediments. Coupling of sediment properties with the mid-to-low sedimentation rates of the area result in minor overpressures ($\lambda^* < 0.1$) before the occurrence of the first flank collapse (Figure 12a). The occurrence of the first two flank collapses and emplacement of Debris Avalanche Deposits (DAD) are dated between 127 and 45 ka, resulting in high overpressures in the easternmost part of the Grenada Basin (Figure 12b). DAD emplacement-induced compaction of the pre-existing sediments and created fluid flow velocities up to 7 times higher than the hydraulic conductivities. Fluid flow-induced pore pressure might reduce the sediment bearing capacity and shear strength favouring its deformation and mobilization into landslides. Thrust and fold structures related to the compressional part of the deformation caused up to 40 m of sediment exhumation, as suggested by the over consolidation state of sediments in borehole U1400. According to onshore dating of the volcano collapse scars (Boudon et al., 2013) and the different scenarios here evaluated, the time gap between DAD1 and DAD2 may be 50 to 80 kyrs. From 127 to 36 ka sea-floor sediments suffered long term deformation driven by the combination of DAD overburden emplaced and persisting high overpressures. This deformation propagated tens of kilometres seaward. The higher the overpressure developed, the higher the deformation/sediment remobilization observed at Present. Although at the time of occurrence of the third flank collapse the overpressures had decreased significantly, emplacement of the DAD3, with a volume two orders of magnitude lower, triggered new overpressure ratio build up (λ^* ca. 0.7) inducing new sediment deformation (Figure 12c). After emplacement of the DAD3 the overpressures decreased to low values. However, it is possible that sediment deformation continues today due to persisting overpressure ratio of 0.1–0.2 (Figure 12d). These overpressures are a key parameter to consider in the geohazard evaluation, and specially in an area with recurrent earthquakes.

ACKNOWLEDGEMENTS

Seismic line RC1504 downloaded from The Academic Seismic Portal at UTIG is a component of the Marine Geoscience Data System (Christeson et al., 2017). This study was supported by the PREST project co-funded by INTERREG Caraïbes for the European Regional Development Fund. We thank ANR-13-BS06-0009 and Labex UnivEarth for funding. We thank reviewers M. Urlaub, E. Lebas and J. Hunt and the Editor, C. Magee, for their critical and helpful reviews that improved the manuscript.

PEER REVIEW

The peer review history for this article is available at https://publons.com/publon/10.1111/bre.12553.

DATA AVAILABILITY STATEMENT

Data from the IODP-340 Expedition and the seismic datasets used are available at: http://iodp.tamu.edu/scienceops/expeditions/antilles_volcanism_landslides.html, http://donnees-campagnes.flotteoceanographique.fr/search.

Uncited references

ORCID

Jaume Llopart https://orcid.org/0000-0002-9495-1194

REFERENCES

Aitken, T., Mann, P., Escalona, A., & Christeson, G. L. (2011). Evolution of the Grenada and Tobago basins and implications for arc migration. *Marine and Petroleum Geology*, *28*, 235–258. https://doi.org/10.1016/j.marpetgeo.2009.10.003

Bitzer, K. (1996). Modeling consolidation sedimentary and fluid basins flow. *Computers & Geosciences*, *22*, 467–478.

Bitzer, K. (1999). Two-dimensional simulation of clastic and carbonate sedimentation, consolidation, subsidence, fluid flow, heat flow and solute transport during the formation of sedimentary basins. *Computers & Geosciences*, *25*, 431–447. https://doi.org/10.1016/S0098-3004(98)00147-2

Boudon, G., Le Friant, A., Komorowski, J. C., Deplus, C., & Semet, M. P. (2007). Volcano flank instability in the Lesser Antilles Arc: Diversity of scale, processes, and temporal recurrence. *Journal of Geophysical Research: Solid Earth*, *112*. https://doi.org/10.1029/2006BJ004674

Boudon, G., Villemant, B., Friant, A. L., Paterne, M., & Cortijo, E. (2013). Role of large flank-collapse events on magma evolution of volcanoes. Insights from the Lesser Antilles Arc. J. Volcanol. Geotherm. Res. *Magma System Response to Edifice Collapse*, *263*, 224–237. https://doi.org/10.1016/j.jvolgeores.2013.03.009

Bouysse, P., Baubron, J. C., Richard, M., Maur, R. C., & Andreieff, P. (1985). Evolution de la terminaison nord de l'arc interne des Petites Antilles au Plio-Quaternaire. *Bulletin De La Société Géologique De France*, *I*, 181–188. https://doi.org/10.2113/gssgfbull.I.2.181

British Standards Institution. (1990). Part 6. Consolidation and permeability test in hydraulic cells and with pore pressure measurement, in: Soils for Civil Engineering Purposes. Road Enineering Satndards Committee, p. 61.

Brunet, M., Le Friant, A., Boudon, G., Lafuerza, S., Talling, P., Hornbach, M., Ishizuka, O., Lebas, E., & Guyard, H. (2016). Composition, geometry, and emplacement dynamics of a large volcanic island landslide offshore Martinique: From volcano flank-collapse to seafloor sediment failure? *Geochemistry, Geophysics, Geosystems*, *17*, 699–724. https://doi.org/10.1002/2015GC006034

Brunet, M., Moretti, L., Le Friant, A., Mangeney, A., Fernández Nieto, E. D., & Bouchut, F. (2017). Numerical simulation of the 30–45 ka debris avalanche flow of Montagne Pelée volcano, Martinique: From volcano flank collapse to submarine emplacement. *Natural Hazards*, *87*(2), 1189–1222. https://doi.org/10.1007/s11069-017-2815-5

Bull, S., Cartwright, J., & Huuse, M. (2009). A review of kinematic indicators from mass-transport complexes using 3D seismic data. *Marine and Petroleum Geology*, *26*, 1132–1151. https://doi.org/10.1016/j.marpetgeo.2008.09.011

Christeson, G., Shipley, T., Gahagan, L., Johnson, K., & Davis, M. (2017). Academic Seismic Portal (ASP) at UTIG [WWW Document]. Univ. Tex. Inst. Geophys. http://www-udc.ig.utexas.edu/sdc/

Cohen, J. K., & Stockwell, J. W. Jr. (1996). Cwp/su release 28, a free seismic software environment for unix platforms.

Deplus, C., Le Friant, A., Boudon, G., Komorowski, J.-C., Villemant, B., Harford, C., Ségoufin, J., & Cheminée, J.-L. (2001). Submarine evidence for large-scale debris avalanches in the Lesser Antilles Arc. *Earth and Planetary Science Letters*, *192*, 145–157. https://doi.org/10.1016/S0012-821X(01)00444-7

Dimakis, P., Elverhøi, A., Høeg, K., Solheim, A., Harbitz, C., Laberg, J. S., Vorren, O., & Marr, J. (2000). Submarine slope stability on high-latitude glaciated Svalbard-Barents Sea margin. *Marine Geology*, *162*(2-4), 303–316. https://doi.org/10.1016/S0025-3227(99)00076-6

Flemings, P., Long, H., Dugan, B., Germaine, J., John, C., Behrmann, J., & Sawyer, D. (2008). Pore pressure penetrometers document high overpressure near the seafloor where multiple submarine landslides have occurred on the continental slope, offshore Louisiana, Gulf of Mexico. *Earth and Planetary Science Letters*, *269*, 309–325. https://doi.org/10.1016/j.epsl.2007.12.005

Frey-Martínez, J., Cartwright, J., & James, D. (2006). Frontally confined versus frontally emergent submarine landslides: A 3D seismic characterisation. *Marine and Petroleum Geology*, *23*, 585–604. https://doi.org/10.1016/j.marpetgeo.2006.04.002

Germa, A., Quidelleur, X., Labanieh, S., Chauvel, C., & Lahitte, P. (2011). The volcanic evolution of Martinique Island: Insights from K-Ar dating into the Lesser Antilles arc migration since the Oligocene. *Journal of Volcanology and Geothermal Research*, *208*, 122–135. https://doi.org/10.1016/j.jvolgeores.2011.09.007

Germa, A., Quidelleur, X., Labanieh, S., Lahitte, P., & Chauvel, C. (2010). The eruptive history of Morne Jacob volcano (Martinique Island, French West Indies): Geochronology, geomorphology and geochemistry of the earliest volcanism in the recent Lesser Antilles arc. *Journal of Volcanology and Geothermal Research*, *198*, 297–310. https://doi.org/10.1016/j.jvolgeores.2010.09.013

Hornbach, M. J., Manga, M., Genecov, M., Valdez, R., Miller, P., Saffer, D., Adelstein, E., Lafuerza, S., Adachi, T., Breitkreuz, C., Jutzeler, M., Le Friant, A., Ishizuka, O., Morgan, S., Slagle, A., Talling, P. J., Fraass, A., Watt, S. F. L., Stroncik, N. A., … Wang, F. (2015). Permeability and pressure measurements in Lesser Antilles submarine slides: Evidence for pressure-driven slow-slip failure. *Journal of Geophysical Research: Solid Earth*, *120*, 7986–8011. https://doi.org/10.1002/2015JB012061

Hurtado, J. E., & Barbat, A. H. (1998). Monte Carlo techniques in computational stochastic mechanics. *Archives of Computational Methods in Engineering*, *5*, 3–29. https://doi.org/10.1007/BF02736747

Ingólfsson, Ó., Benediktsson, Í. Ö., Schomacker, A., Kjær, K. H., Brynjólfsson, S., Jónsson, S. A., Korsgaard, N. J., & Johnson, M. D. (2016). Glacial geological studies of surge-type glaciers in Iceland — Research status and future challenges. *Earth Science Reviews*, *152*, 37–69. https://doi.org/10.1016/j.earscirev.2015.11.008

Krastel, S., Schmincke, H.-U., Jacobs, C. L., Rihm, R., Bas, T. P. L., & Alibés, B. (2001). Submarine landslides around the Canary Islands. *Journal of Geophysical Research: Solid Earth*, *106*, 3977–3997. https://doi.org/10.1029/2000JB900413

Lafuerza, S., Le Friant, A., Manga, M., Boudon, G., Villemant, B., Stroncik, N., Voight, B., Hornbach, M., & Ishizuka, O. (2014). Geomechanical characterization of submarine volcano-flank sediments, martinique, lesser antilles arc. In G. Lamarche, J. Mountjoy, S. Bull, T. Hubble, S. Krastel, E. Lane, A. Micallef, L. Moscardelli, C. Mueller, I. Pecher, & S. Woelz (Eds.), *Submarine mass movements and their consequences, advances in natural and technological hazards research* (pp. 73–81). Springer International Publishing. https://doi.org/10.1007/978-3-319-00972-8_7

Le Friant, A., Boudon, G., Deplus, C., & Villemant, B. (2003). Large-scale flank collapse events during the activity of Montagne Pelée, Martinique, Lesser Antilles. *J Journal of Geophysical Research: Solid Earth*, *108*, 1–15. https://doi.org/10.1029/2001JB001624

Le Friant, A., Boudon, G., Komorowski, J. C., & Deplus, C. (2002). L'île de la Dominique, à l'origine des avalanches de débris les plus volumineuses de l'arc des Petites Antilles. *Comptes Rendus Geoscience*, *334*, 235–243. https://doi.org/10.1016/S1631-0713(02)01742-X

Le Friant, A., Ishizuka, O., Boudon, G., Palmer, M. R., Talling, P. J., Villemant, B., Adachi, T., Aljahdali, M., Breitkreuz, C., Brunet, M., Caron, B., Coussens, M., Deplus, C., Endo, D., Feuillet, N., Fraas, A. J., Fujinawa, A., Hart, M. B., Hatfield, R. G., … Watt, S. F. L. (2015). Submarine record of volcanic island construction and collapse in the Lesser Antilles arc: First scientific drilling of submarine volcanic island landslides by IODPExpedition 340.

Geochemistry, Geophysics, Geosystems, *16*, 420–442. https://doi.org/10.1002/2014GC005652

Le Friant, A., Lebas, E., Clément, V., Boudon, G., Deplus, C., De Voogd, B., & Bachlery, P. (2011). A new model for the evolution of la Reunion volcanic complex from complete marine geophysical surveys. *Geophysical Research Letters*, *38*, 6–11. https://doi.org/10.1029/2011GL047489

Lebas, E., Le Friant, A., Boudon, G., Watt, S. F. L., Talling, P. J., Feuillet, N., Deplus, C., Berndt, C., & Vardy, M. E. (2011). Multiple widespread landslides during the long-term evolution of a volcanic island: Insights from high-resolution seismic data, Montserrat, Lesser Antilles. *Geochemistry, Geophysics, Geosystems*, *12*(5). https://doi.org/10.1029/2010GC003451

Le Friant, A., Ishizuka, O., Stroncik, N. A., & Scientists, E. 340, 2013a. Proc. IODP, 340, Proceedings of the IODP. Integrated Ocean Drilling Program, Tokyo.

Le Friant, A., Ishizuka, O., Stroncik, N. A., & Scientists, E. 340, 2013b. 340, 2013b. Proc. IODP, 340, Proceedings of the IODP. Integrated Ocean Drilling Program, Tokyo.

Llopart, J., Urgeles, R., Forsberg, C. F., Camerlenghi, A., Vanneste, M., Rebesco, M., Lucchi, R. G., Rüther, D. C., & Lantzsch, H. (2019). Fluid flow and pore pressure development throughout the evolution of a trough mouth fan, western Barents Sea. *Basin Research*, 1–27. https://doi.org/10.1111/bre.12331

Lunne, T., Berre, T., Andersen, K. H., Strandvik, S., & Sjursen, M. (2006). Effects of sample disturbance and consolidation procedures on measured shear strength of soft marine Norwegian clays. *Canadian Geotechnical Journal*, *43*, 726–750. https://doi.org/10.1139/t06-040

Masson, D. G., Harbitz, C. B., Wynn, R. B., Pedersen, G., & Lvholt, F. (2006). Submarine landslides: Processes, triggers and hazard prediction. *Philosophical Transactions of the Royal Society A: Mathematical, Physical and Engineering Sciences*, *364*(1845), 2009–2039.

Micallef, A., Masson, D. G., Berndt, C., & Stow, D. A. (2009). Development and mass movement processes of the north-eastern Storegga Slide. *Quaternary Science Reviews*, *28*, 433–448. https://doi.org/10.1016/j.quascirev.2008.09.026

Moernaut, J., & De Batist, M. (2011). Frontal emplacement and mobility of sublacustrine landslides: Results from morphometric and seismostratigraphic analysis. *Marine Geology*, *285*, 29–45. https://doi.org/10.1016/j.margeo.2011.05.001

Moore, J. G., Normark, W. R., & Holcomb, R. T. (1994). Giant hawaiian landslides. *Annual Review of Earth and Planetary Sciences*, *22*, 119–144. https://doi.org/10.1146/annurev.ea.22.050194.001003

Nadim, F. (2015). Accounting for Uncertainty and Variability in Geotechnical Characterization of Offshore Sites. In T. Schweckendiek, A. F. Van Tol, D. Pereboom, A. Van Staveren, & P. M. C. B. M. Cools (Eds.), *Geotechnical safety and risk V* (23–34). IOS Press. https://doi.org/10.3233/978-1-61499-580-7-23

Nilsson, B., Højberg, A. L., Refsgaard, J. C., & Troldborg, L. (2007). Uncertainty in geological and hydrogeological data. *Hydrology and Earth System Sciences*, *11*, 1551–1561. https://doi.org/10.5194/hess-11-1551-2007

Oehler, J.-F., Lénat, J.-F., & Labazuy, P. (2008). Growth and collapse of the Reunion Island volcanoes. *Bulletin of Volcanology*, *70*, 717–742. https://doi.org/10.1007/s00445-007-0163-0

Poulain, P., Le Friant, A., Mangeney, A., Viroulet, S., Fernandez-Nieto, E., Castro Diaz, M. J., Peruzzetto, M., Bouchut, F., & Grandjean, G. (2020). Submarine granular flows and generated tsunami waves: from laboratory experiments to numerical simulations of Montagne Pelée flank collapses. *Journal of Geophysical Research: Earth Surface*.

Puzrin, A. M., Germanovich, L. N., & Friedli, B. (2016). Shear band propagation analysis of submarine slope stability. *Géotechnique*, *66*, 188–201. https://doi.org/10.1680/jgeot.15.LM.002

Reid, R. P., Carey, S. N., & Ross, D. R. (1996). Late Quaternary sedimentation in the Lesser Antilles island arc. *GSA Bull.*, *108*, 78–100. https://doi.org/10.1130/0016-7606(1996)108<0078:LQSITL>2.3.CO;2

Solaro, C., Boudon, G., Le Friant, A., Balcone-Boissard, H., Emmanuel, L., & Paterne, M. (2020). New insights into the recent eruptive and collapse history of Montagne Pelée (Lesser Antilles Arc) from offshore marine drilling site U1401A (IODP Expedition 340). *Journal of Volcanology and Geothermal Research*, *403*, 107001. https://doi.org/10.1016/j.jvolgeores.2020.107001

Talwani, M., Windisch, C. C., Stoffa, P. L., Buhl, P., & Houtz, R. (1977). Multichannel seismic study in the Veneuzela n B asin and the Curac aoRidge. In: M. Talwani, & W. C. Pitman III (Eds.), *Island Arcs, Deep Sea Trenches and Back-Arc Basins, MauriceEwing Ser* (pp. 83–98). AGU.

Urgeles, R., Masson, D. G., Canals, M., Watts, A. B., & Le Bas, T. (1999). Recurrent large-scale landsliding on the west flank of La Palma, Canary Islands. *Journal of Geophysical Research: Solid Earth*, *104*, 25331. https://doi.org/10.1029/1999JB900243

Urlaub, M., Talling, P. J., & Masson, D. G. (2013). Timing and frequency of large submarine landslides: Implications for understanding triggers and future geohazard. *Quaternary Science Reviews*, *72*, 63–82. https://doi.org/10.1016/j.quascirev.2013.04.020

Van Daele, M., Versteeg, W., Pino, M., Urrutia, R., & De Batist, M. (2013). Widespread deformation of basin-plain sediments in Aysén fjord (Chile) due to impact by earthquake-triggered, onshore-generated mass movements. *Marine Geology*, *337*, 67–79. https://doi.org/10.1016/j.margeo.2013.01.006

Van Hinte, J. E. (1978). Geohistory analysis; application of micropaleontology in exploration geology. *AAPG Bull.*, *62*, 201–222.

Vincent, P. M., Bourdier, J. L., & Boudon, G. (1989). The primitive volcano of Mount Pelée: Its construction and partial destruction by flank collapse. *Journal of Volcanology and Geothermal Research*, *38*, 1–15. https://doi.org/10.1016/0377-0273(89)90026-7

Watson, S. J., Whittaker, J. M., Lucieer, V., Coffin, M. F., & Lamarche, G. (2017). Erosional and depositional processes on the submarine flanks of Ontong Java and Nukumanu atolls, western equatorial Pacific Ocean. *Marine Geology*, *392*, 122–139. https://doi.org/10.1016/j.margeo.2017.08.006

Watt, S. F. L., Talling, P. J., Vardy, M. E., Heller, V., Hühnerbach, V., Urlaub, M., Sarkar, S., Masson, D. G., Henstock, T. J., Minshull, T. A., Paulatto, M., Le Friant, A., Lebas, E., Berndt, C., Crutchley, G. J., Karstens, J., Stinton, A. J., & Maeno, F. (2012). Combinations of volcanic-flank and seafloor-sediment failure offshore Montserrat, and their implications for tsunami generation. *Earth and Planetary Science Letters*, *319–320*, 228–240. https://doi.org/10.1016/j.epsl.2011.11.032

Watt, S. F. L., Talling, P. J., Vardy, M. E., Masson, D. G., Henstock, T. J., Hühnerbach, V., Minshull, T. A., Urlaub, M., Lebas, E., Le Friant, A., Berndt, C., Crutchley, G. J., & Karstens, J. (2012). Widespread and progressive seafloor-sediment failure following volcanic debris avalanche emplacement: Landslide dynamics and timing offshore Montserrat, Lesser Antilles. *Marine Geology*, *323–325*, 69–94. https://doi.org/10.1016/j.margeo.2012.08.002

Westercamp, D., d'Archimbaud, J. D., de Lapparent, A. F., Marinelli, G., Tazieff, H., & Brousse, R. (1972). Contribution à l'étude du volcanisme en Martinique. éditeur non identifié.

Westercamp, D., Pelletier, B., Thibaut, P., Traineau, H., & Andreieff, P. (1990). Carte géologique de la France (1/50 000), feuille Martinique.

Williams, R., Rowley, P., & Garthwaite, M. C. (2019). Reconstructing the Anak Krakatau flank collapse that caused the December 2018 Indonesian tsunami. *Geology*, *47*, 973–976. https://doi.org/10.1130/G46517.1

SUPPORTING INFORMATION

Additional supporting information may be found online in the Supporting Information section.

How to cite this article: Llopart J, Lafuerza S, Le Friant A, Urgeles R, Watremez L. Long-term and long-distance deformation in submarine volcanoclastic sediments: Coupling of hydrogeology and debris avalanche emplacement off W Martinique Island. *Basin Res*. 2021;00:1–23. https://doi.org/10.1111/bre.12553

Graphical Abstract

The contents of this page will be used as part of the graphical abstract of html only. It will not be published as part of main article.

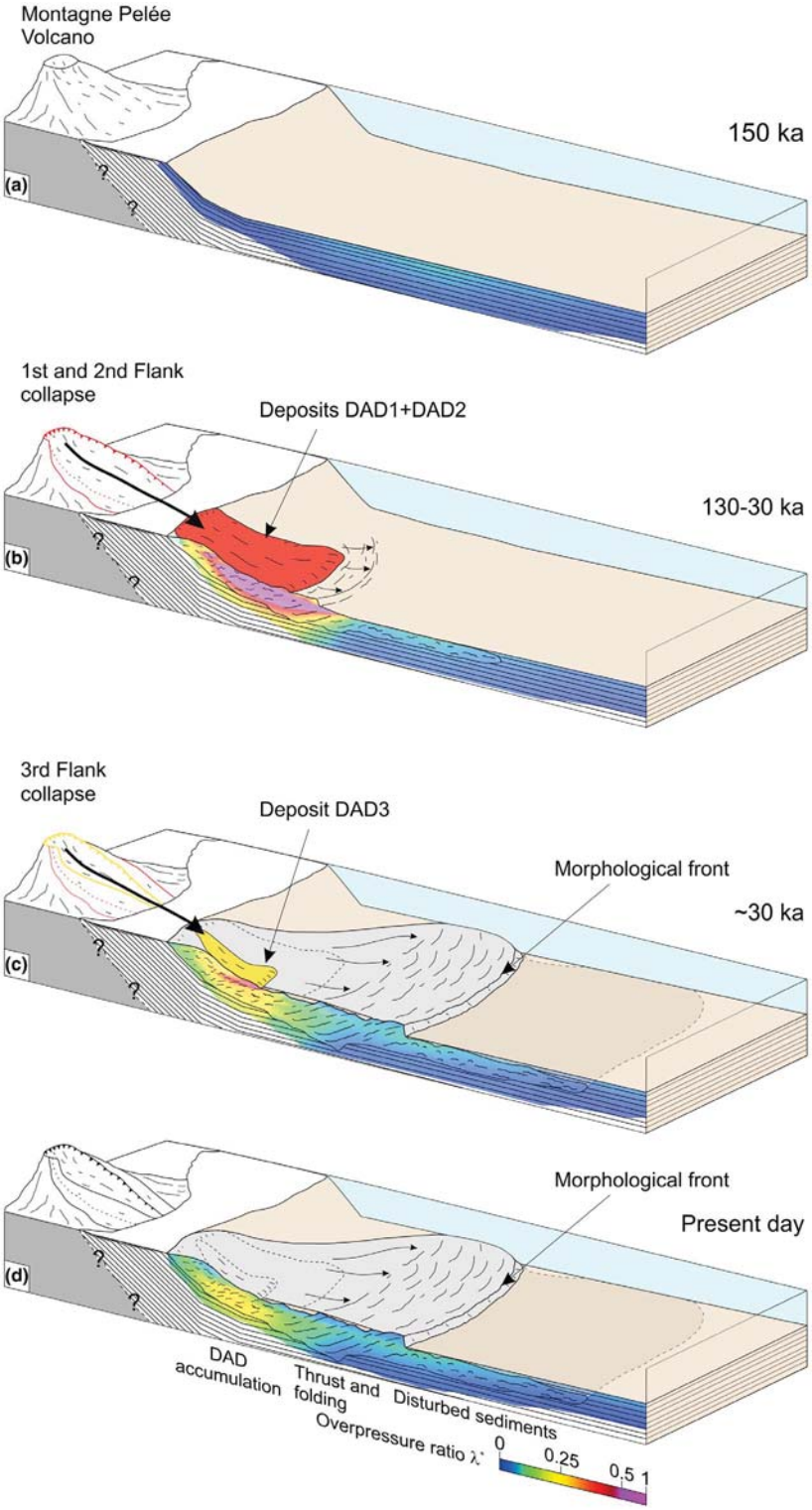

XXX.